

Magnetic dipole moments as a strong signature for α -clustering in even-even self-conjugate nuclei

Gianluca Stellin^{a,b,c,d}, Karl-Heinz Speidel^a, Ulf-G. Meißner^{a,b,e,f}

^a*Helmholtz Institut für Strahlen- und Kernphysik, Universität Bonn, Nußallee 14-16, 53115 Bonn, Germany*

^b*Bethe Center for Theoretical Physics, Universität Bonn, Nußallee 12, 53115 Bonn, Germany*

^c*DRF/IRFU/DPhN/LENA, CEA Paris-Saclay, Bât. 703, 91190 Saint-Aubin, France*

^d*Espace de Structure Nucleaire Théorique, CEA Paris-Saclay, Bât. 703, 91190 Saint-Aubin, France*

^e*Institute for Advanced Simulation, Institut für Kernphysik and Jülich Center for Hadron Physics, Forschungszentrum Jülich, 52425 Jülich, Germany*

^f*Ivane Javakhishvili Tbilisi State University, 0186 Tbilisi, Georgia*

Abstract

We investigate the magnetic dipole moments in even-even self-conjugate nuclei from ^{12}C to ^{44}Ti . For the latter, the measured gyromagnetic factors of excited states turn out to assume the same value of $g \approx +0.5$ within statistical errors. This peculiar feature can be interpreted on the basis of collective excitations of α -clusters. Analogously, the behaviour of the same observable is studied for all isotopes obtained by adding one or two neutrons to the considered self-conjugate nuclei. It is found that for the $N = Z + 1$ isotopes the α -cluster structure hardly contributes to the observed negative g -factor value, corroborating molecular α -cluster models. The addition of a further neutron, however, restores the original α -cluster g -factors, except for the semi-magic isotopes, in which the deviations from $g \approx +0.5$ can be associated with the relevant shell closures. Secondly, we analyze the same observable in the framework of a macroscopic α -cluster model on a finite lattice of side length L . We focus on the discretization effects induced in the magnetic dipole moments of the 2_1^+ and the 3_1^- states of ^{12}C at different values of the lattice spacing a .

Keywords: Electromagnetic Procs. and Props., Nucl. Struct. Mod. and Meth., Few-Body Syst.

PACS: 12.38.Gc, 21.60.-n, 25.45.-v

Contents

1	Preamble	2
2	Magnetic dipole moments	3
2.1	$N = Z$ nuclei	4
2.2	$N = Z + 1$ nuclei	7
2.3	$N = Z + 2$ nuclei	11
3	The ^{12}C nucleus	16
4	Conclusion	25
	Appendices	26

1. Preamble

The tendency of nucleons to congregate into clusters is known since the early days of nuclear physics [1]. The intrinsic stability of the ${}^4\text{He}$ nucleus alongside with the energy gap of 20.21 MeV with respect to the lowest single-particle excited state, makes the α -particle a candidate for a conglomerate of nucleons capable of surviving relatively unperturbed within the nuclear mean field, for a recent review see [2]. It is in fact well established that nuclear spectra are a result of the interplay between pairing and cluster correlations and the mean field generated by the individual nucleons [3]. In absence of correlations between the constituents, nucleons would move as independent particles and a well-pronounced shell structure (the Fermi surface) would appear [3]. As soon as the residual attractive interactions are turned on, nucleons orbiting in the same subshell but with opposite projection of the angular momentum along the symmetry axis of the nucleus (i.e. connected by the antiunitary time-reversal operation, see refs. [4, 5]) form Cooper pairs [6, 7] or give rise to larger subsystems. Among the latter, the α -particle dominates in nuclei with even and equal numbers of protons and neutrons, whose higher binding energy per nucleon reaches a local maximum in the Segrè chart. Cluster correlations are found to reduce the neutron skin thickness with respect to a mean field value [8].

Additionally, in the pioneering work in ref. [9] it was noticed that the binding energies of light α -conjugate nuclei scale linearly with the number of bonds among the α -clusters, sitting at the vertices of regular polyhedra (cf. fig. 1 in ref. [10] and refs. [11, 12, 13]). In particular, the adoption of the equilateral triangle (\mathcal{D}_{3h}) [14, 15, 16], the tetrahedron (\mathcal{T}_d) and the triangular bipyramid (\mathcal{D}_{3h}) as basis-configuration for the inspection of the structure properties of the ${}^{12}\text{C}$ [17] and ${}^{16}\text{O}$ [18, 19] within the Algebraic Cluster Model (ACM) [12, 20] and of the ${}^{20}\text{Ne}$ [21] within a geometric macroscopic α -cluster model, respectively, has revived the interest for the subject in recent times (cf. refs. [22, 23]).

Furthermore, α -clustering is reinforced as the excitation energy grows. As an example, in ${}^{12}\text{C}$ at around 10 MeV the nuclear density reduces to less than one third with respect to the initial value (cf. refs. [23]) and the inter- α separation increases accordingly. An example is represented by the Hoyle state at 7.65 MeV, credited by microscopic studies as a triangular *bent-arm* arrangement of α -particles [24, 25] and earlier as a linear chain configuration [26]. On the other hand, the triangular ground state keeps a significant overlap with the $p_{3/2}$ closed subshell configuration (cit. refs. [3]), as the independent-particle in a mean field feature gains ground. In the opposite limit, the nucleus dissociates completely into the twelve constituents at around 10^2 MeV [3].

The idea according to which the α -particle structure is not manifest in the ground state but emerges gradually with the increase of the internal energy of the system is at the origin of the diagrammatic representation proposed in refs. [27, 28] for the ${}^{12}\text{C}$, ${}^{16}\text{O}$, ${}^{20}\text{Ne}$, ${}^{24}\text{Mg}$ and ${}^{28}\text{Si}$ nuclei. The ensuing *Ikeda diagram* predicts fully-clustered states, i.e. $M\alpha$ -cluster configurations with $2M = Z = N$, only in the correspondence of the $M\alpha$ -breakup thresholds.

Therefore, the adoption of pictures that neglect the inner degrees of freedom of the ${}^4\text{He}$

clusters for the analysis of excited state properties, such as intrinsic magnetic dipole moments, of this class of nuclei appears justified. Motivated by the long standing experimental interest in magnetic moments for ^{12}C [29], ^{16}O [30], ^{20}Ne [31], ^{24}Mg [32], ^{28}Si [33], ^{32}S [34], ^{36}Ar [33], ^{40}Ca [35, 36] and ^{44}Ti [37], this paper is dedicated to the theoretical interpretation of these observables throughout light and medium-mass α -conjugate nuclei. Moreover, we point out that in part of the aforementioned bibliography, e.g. the measurement of the g-factor of the 3_1^- state of ^{16}O in ref. [30], the α -cluster nature that characterizes this nucleus was marginalized if not ignored during the discussion of the observed data.

The primary target of the present article is to fill this gap in the literature, showing that experimental g-factor values lie in a reasonable neighbourhood of $g = +0.5$ and constitute a new unambiguous evidence for an α -cluster structure in even-even self-conjugate nuclei. In particular, the treatment begins with the presentation of the values of the g-factors for low-lying energy levels of light and medium mass nuclei computed in the framework of the nuclear shell model (cf. ref. [38]). In parallel, we extract for comparison the same quantities by means of the Schmidt estimates [39, 40]. Subsequently, we repeat the calculation by adding one or two neutrons to the original nuclei, highlighting how this operation alters the g-factor values. We further contextualize the outcoming nuclides in the realm of *molecular nuclei* [3, 41, 42], where the added neutron(s) either assume the role of valence particles (e.g. ^{10}Be) [3] or become an integral part of the cluster themselves (e.g. ^{12}Be) [3].

Secondly, the recent experimental advances as well as the surge of interest for α -conjugate nuclei calls for a study of magnetic dipole moments, μ , and g-factors in the framework of purely α -cluster models as the one in refs. [43, 44] on a cubic lattice. In particular, we display the behaviour of the average value of μ computed on the 2_1^+ and 3_1^- states of ^{12}C with maximum angular momentum projection as a function of the lattice spacing. Moreover, in sec. 3 we demonstrate, how multiplet averaged [44] and isotropically averaged [45] values of the latter observable succeed in reducing the artifacts associated with finite lattice spacing in the two energy levels of the same nucleus recently analysed in ref. [46].

2. Magnetic dipole moments

Magnetic dipole moments are known to contain information on the microscopic structure of a nuclear system. These observables are indeed very sensitive to the occupancy of quasiparticle orbits of valence nucleons and serve as a testing ground for A -body wavefunctions and theoretical models in general. Besides, the measurement of the magnetic dipole moments represents an immediate verification for the assignment of a given angular momentum to nuclear ground and excited states in the shell model. In the many-body definition (cf. ref. [47, 48]), the former are given by the superposition of the single-nucleon orbital angular momentum and spin operators [48],

$$\boldsymbol{\mu} = \frac{e}{2m_p} \sum_{\pi=1}^Z (g_\ell^\pi \boldsymbol{\ell}_\pi + g_s^\pi \mathbf{s}_\pi) + \frac{e}{2m_n} \sum_{\nu=1}^N (g_\ell^\nu \boldsymbol{\ell}_\nu + g_s^\nu \mathbf{s}_\nu) , \quad (1)$$

weighted by the spin and orbital gyromagnetic factors indexed by π (ν) for protons (neutrons). Here, e denotes the unit electromagnetic charge and m_n and m_p the mass of the neutron and the proton, in order. For *free* nucleons in ref. [49] the g-factors assume the values

$$\begin{aligned} g_\ell^p &= 1 & g_s^p &= 5.5856946893(16) , \\ g_\ell^n &= 0 & g_s^n &= -3.82608545(90) . \end{aligned} \quad (2)$$

In more refined calculations, g_s^p and g_s^n are quenched by a factor $0.60 \div 0.75$ [50, 51] in order to account for the polarization of the core of the nucleus and for the meson-exchange current (MEC) corrections [52]. Nonetheless, some authors [53] prefer to neglect these corrections and use the free values for charges and g-factors of nucleons in the microscopic calculations of electromagnetic moments and transition probabilities. Ab-initio estimates for the corrections to the g-factors can be extracted from the average values of the MECs in the zero-momentum-transfer limit in eq. (125) of ref. [54], derived in the framework of chiral effective field theory (χ EFT). Note that the currents used by these authors have to be taken with a grain of salt [55]. For the Schmidt estimates (SE) presented in this section, we reduce the nucleon g-factors to 70 % of the free values and assume Z to be always even.

2.1. $N = Z$ nuclei

We target the average values of the operator in eq. (1) in low-energy excited states of α -conjugate nuclei. Motivated by the high stability of the ${}^4\text{He}$ nucleus, we suppress the single-nucleon degrees of freedom in spite of the former accomplishment and interpret the nuclear excitations in terms of the rotational and vibrational motion of the $M \equiv Z/2$ α -particles. These bosonic groupings are characterized by zero spin and isospin as well as vanishing magnetic dipole moment in the 0^+ ground state. In such a *macroscopic* framework, the spin contribution to the magnetic dipole moment remains equal to zero in any excited state. Hence, we are allowed to set $g_s^\alpha = 0$ and rewrite eq. (1) as

$$\boldsymbol{\mu}^{(\alpha)} = \frac{e}{2m_\alpha} \sum_{i=1}^M g_\ell^\alpha \boldsymbol{\ell}_i = \frac{e}{2m_p} g_L^{(\alpha)} \mathbf{L} , \quad (3)$$

where m_α is the α -particle mass, the summation is performed over the M α -clusters, $g_\ell^\alpha = 2$ is the orbital component of the gyromagnetic factor for the α -particle and

$$g_L^{(\alpha)} \equiv g_\ell^\alpha \frac{m_p}{m_\alpha} = \frac{2m_p}{m_\alpha} \approx +0.5034 , \quad (4)$$

coincides with the nuclear g-factor. Its small deviation with respect to 0.5 is essentially due to the mass excess of the ${}^4\text{He}$ nucleus.

The available experimental values for $g_L^{(\alpha)}$ in light and medium-mass $N = Z$ even-even self-conjugate nuclei are all compatible within the statistical errors with the outcome of eq. (3) for macroscopic models. This remarkable agreement emerges dramatically in fig. 1 and constitutes the cornerstone of the present interpretation. The validity of this assertion is not limited to the lowest 2^+ or 3^- states of α -conjugate nuclei, but remains intact at growing excitation energies.

NUCLEUS	LEVEL	ENERGY [MeV]	$g^{(SM)}$	$g^{(\alpha)}$	$g^{(exp)}$	Z/A
^8Be	2_1^+	3.030	—	+0.5034	—	+0.50
^{12}C	2_1^+	4.438	+0.507 [56]	+0.5034	+0.60(20) [29]	+0.50
^{16}O	3_1^-	6.130	+0.555 [56]	+0.5034	+0.556(4) [30]	+0.50
^{20}Ne	2_1^+	1.634	+0.510 [57]	+0.5034	+0.54(4) [58]	+0.50
	4_1^+	4.247	+0.513 [57]		+0.43(9) [59]	
^{24}Mg	2_1^+	1.369	+0.513 [57]	+0.5034	+0.538(13) [60]	+0.50
	4_1^+	4.123	+0.518 [57]		+0.40(30) [61]	
	2_2^+	4.238	+0.519 [57]		+0.60(20) [61]	
	4_2^+	6.010	+0.512 [57]		+0.50(40) [62]	
^{28}Si	2_1^+	1.779	+0.516 [57]	+0.5034	+0.53(2) [58]	+0.50
^{32}S	2_1^+	2.230	+0.505 [57]	+0.5034	+0.50(3) [58]	+0.50
	4_1^+	4.459	+0.507 [57]		+0.40(15) [63]	
^{36}Ar	2_1^+	1.970	+0.488 [64]	+0.5034	+0.52(18) [64]	+0.50
^{40}Ca	3_1^-	3.737	+0.486 [69]	+0.5034	+0.52(10) [36]	+0.50
	5_1^-	4.492	+0.512 [69]		+0.52(9) [36]	
^{44}Ti	2_1^+	1.083	+0.514 [37]	+0.5034	+0.52(15) [37]	+0.50

Table 1: Experimental nuclear g-factors for excited states of the lightest α -conjugate nuclei (exp) with the predictions of the shell model (SM), the macroscopic α -cluster models (α) and the collective Z/A value.

Exemplary, in this respect, is the case of the 2_1^+ and the 4_1^+ levels of ^{20}Ne and ^{32}S as well as the 2_1^+ , 4_1^+ , 2_2^+ and 4_2^+ states of ^{24}Mg , where the measured g-factors do not display systematic deviations from the value in eq. (3) within their sizable errors (cf. tab. 1). In the framework of the shell-model (SM), g-factor values in reasonable neighbourhood of the macroscopic α -cluster value of $\approx +0.5034$ are found. For $10 \leq Z \leq 16$ nuclei the theoretical SM data are obtained through the phenomenological USDB interactions [65], taylored for sd -shell nuclei [66, 67]. Conversely, for ^{36}Ar the WBT interaction in ref. [68] is used in the same model space, whereas for ^{40}Ca the calculations [69] assume admixtures of random phase approximation $1p$ - $1h$ states and deformed $3p$ - $3h$ states [75]. However, the SM configuration $d_{3/2}^{-1}f_{7/2}$ alone yields in ^{40}Ca g-factors in fair agreement with the experimental and large-scale theoretical estimates in ref. [69]. Eventually, for ^{44}Ti the FPD6 [70] nucleon-nucleon interaction is implemented in the full pf -shell model space, assuming a self-conjugate ^{40}Ca core [37].

Furthermore, for states of zero total isospin, as the bosonic ones, generated by excitations of α -particles (cf. tab. 1), the g-factor is predicted to correspond to its isoscalar component,

$$g_J^{(0)} = \frac{\mu_J(T_z = +T) + \mu_J(T_z = -T)}{\mu_N 2J} = \frac{g_\ell^n + g_\ell^p}{2} + \frac{g_s^n + g_s^p - g_\ell^n - g_\ell^p}{2J} \langle S_z \rangle_J \quad (5)$$

where μ_N is the nuclear magneton and $\mu_J(T_z = \pm T)$ are the magnetic dipole moments of two states with total angular momentum J and opposite z-component of the total isospin, *i.e.* mirror

nuclei. In eq. (5), the charge dependence of nuclear force and the nucleon masses has been also ignored, as in eq. (3.2) of ref. [71]. The average value of S_z in the former equation is computed among the states with maximum total angular momentum and isospin projection along the z -axis, $|J, J_z = J, T, T_z = T\rangle$.

Moreover, for purely collective excitations constructed on the $J = 0$ ground state, the total angular momentum coincides with \mathbf{L} and the average value of the third component of the spin in eq. (3.2) of ref. [71] vanishes. As a consequence, the isoscalar part of the gyromagnetic factor becomes independent on J and reduces to $1/2$ [72] (cf. eq. (2)). This result agrees with eq. (3), the deviations owing to the neglected charge dependence of nuclear forces and nucleon masses.

Although the original measurements of the gyromagnetic factors of the 3_1^- state of ^{16}O and the 2_1^+ state of ^{24}Mg yielded $g = +0.55(3)$ [73] and $+0.51(2)$ [74], respectively, the more recent and more precise observations in refs. [30] and [60] highlight a 10 % deviation from the macroscopic α -cluster value in eq. (3). This bias is only marginally covered by the shell-model calculations in ref. [76], where configuration mixing among one-body states lying within major harmonic oscillator shells has been considered.

Nevertheless, in ref. [56] the rest of the discrepancy is successfully attributed to *isospin mixing* exerted by the $T = 1$ (isovector) 3_4^- state at 13.26 MeV, whose reduced magnetic dipole transition probability to the 3_1^+ state is large. Interpreting the two 3^- states as an admixture of $1p$ - $1h$ neutron and proton states of an α -particle such as $p_{1/2}^{-1}d_{5/2}$ and indentifying the mixing source with the Coulomb force V_C , an isovector contribution with the expected magnitude is obtained,

$$g_J^{(1)} = \frac{\mu_J(T_z = +T) - \mu_J(T_z = -T)}{\mu_N 2J} \stackrel{^{16}\text{O } 3_1^-}{\approx} -\frac{2}{3} \frac{\langle 3^-, 1 | \mu_z | 3^-, 0 \rangle}{\mu_N} \frac{\langle 3^-, 0 | V_C | 3^-, 1 \rangle}{|\Delta E_{3-}|}, \quad (6)$$

where $|\Delta E_{3-}|$ denotes the energy separation between the two levels and the compact notation $|J, T\rangle \equiv |JTJ_zT_z\rangle$ for the shell-model states is understood. In summary, the full gyromagnetic factor of the 3_1^- state, $g_J^{(0)} + g_J^{(1)}$, becomes $+0.555$ [56]. The same considerations, applied to the 2_1^+ ($T = 0$) state at 4.44 MeV and the 2_4^+ ($T = 1$) state at 16.11 MeV of ^{12}C , result in a smaller isovector correction to the g-factor of about 1.5 % with respect to the shell-model value (cf. tab. 1). Altogether, the main nuclear structure lends weight to the consistency of α -clustering.

Concerning the 2_1^+ state of ^{24}Mg , the gyromagnetic factor from the USDB Hamiltonian in ref. [65], together with the isovector correction (cf. ref. [77]) yields $+0.520$, is consistent with the most recent experimental counterpart [32]. The overlap improves when also the effects of the MECs on the bare nucleon g-factors in eq. (2) are included [78], leading to a final value of $+0.544$ [32]. For the other values of the gyromagnetic factors reported in tab. 1, times are not ripe for singling out possible deviations from the macroscopic α -cluster value in eq. (3), since the statistical errors affecting the measurements overcome on average the 10 % of the g-factor value itself.

Despite the sizable experimental errors affecting the available estimates and the small deviations from $g_J^{(0)}$, our α -cluster interpretation of the g-factors for this class of nuclei remains solid. Underpinning this construction is the gradual emergence of α -clustering at increasing excitation

energy and, remarkably, close to α -decay thresholds [27]. Although yet unmeasured, the magnetic moments of the 3_1^- and the 2_2^+ states of ^{12}C as well as the 3_5^- and 5_1^+ states of ^{16}O in the close vicinity of the 3α - and 4α -decay thresholds, respectively, are expected to adhere even more faithfully with the predictions of the macroscopic α -cluster picture.

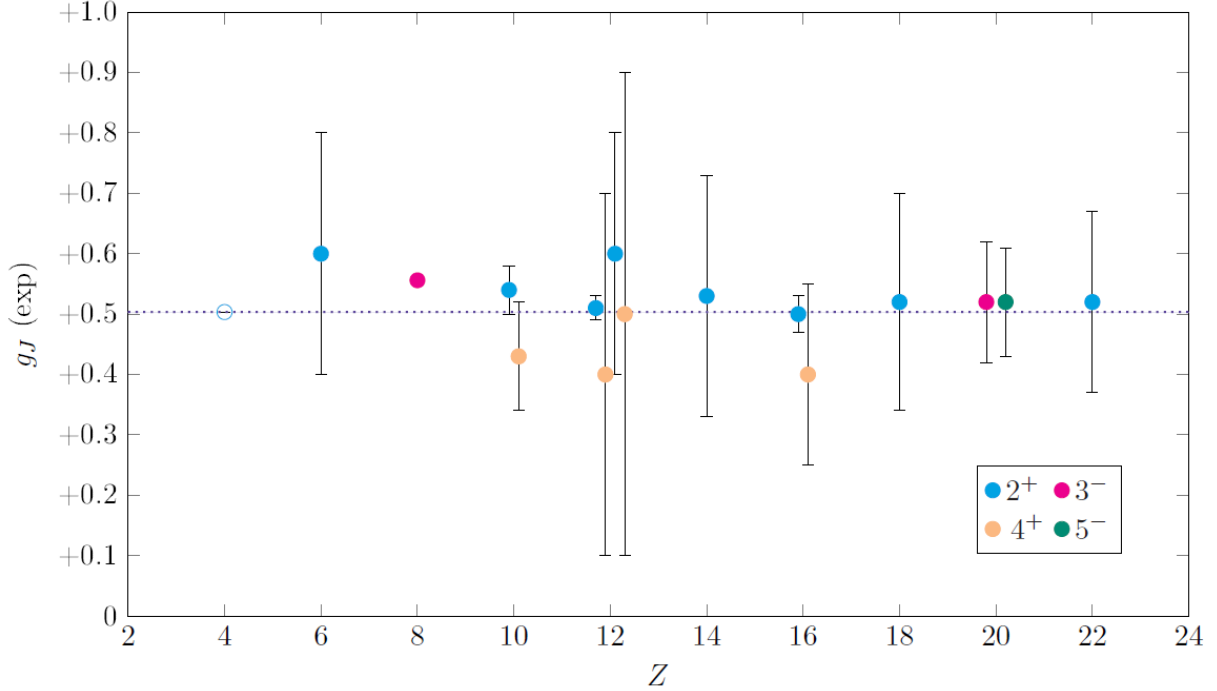


Figure 1: Behaviour of the experimental g-factor values as a function of the proton number for excited states of α -conjugate nuclei. The dotted line denotes the prediction from macroscopic α -cluster models. For the nuclei ^{20}Ne , ^{24}Mg , ^{32}S and ^{40}Ca an artificial shift in the Z direction is added in order to resolve the error bars. The theoretical α -cluster value for the 2_1^+ state of ^8Be is denoted with an open circle (cf. tab. 1)

Besides, as shown in sec. 2.2, the observed independence of the g-factors on the angular momentum and the excitation energy of the states to which they refer, is a peculiar feature, which the $N = Z + 1$ and $Z + 2$ nuclei with even Z do not preserve.

2.2. $N = Z + 1$ nuclei

In the following we consider the case in which a single neutron is added to an α -conjugate nucleus. The major question that naturally arises is whether the additional neutron enhances or weakens α -clustering. Although no general answer exists [3], clustered states are expected to appear in correspondence of the $M\alpha + n$ decay thresholds. For ^9Be , different approaches such as the linear combination of atomic orbitals (LCAO) [79] and the cluster shell model (CSM) [80] highlight an underlying dumbbell configuration with the added neutron moving in the cluster field with Z_2 symmetry [80].

Concerning ^{13}C , the states with excitation energy lying between 9.90 and 16.95 MeV are well reproduced by a molecular α -cluster model [81], in which the odd neutron lies between the ^4He

nuclei arranged in a linear chain. Besides, for the $(1/2)_2^-$ and $(1/2)_1^+$ states of the same nucleus, the triangular α -cluster configuration with one neutron located in the same plane of the ${}^4\text{He}$ nuclei (π -orbit) and along the axis perpendicular to the 3α -plane (σ -orbit), respectively, has been proposed [81]. Additionally, the large isoscalar reduced electric monopole transition probability between the $(1/2)_2^-$ and $(1/2)_3^-$ states and the ground state [82] is also regarded as a signature of α -clustering in this nucleus [41]. Indeed, states lying below the ${}^9\text{Be}+\alpha$ decay threshold are well predicted by the shell-model for p -shell nuclei [83].

NUCLEUS	LEVEL	ENERGY [MeV]	$g^{(SM)}$	$g^{(SE)}$	$g^{(exp)}$	Z/A
${}^9\text{Be}$	$\frac{3}{2}_1^-$	0.0	-0.713 [91]	-0.89	-0.784955(2) [92]	+0.444
${}^{13}\text{C}$	$\frac{1}{2}_1^-$	0.0	+1.506 [91]	+0.89	+1.404824(2) [93]	+0.462
	$\frac{5}{2}_1^+$	3.854	-0.597 [91]	-0.77	-0.59(5) [94]	+0.462
${}^{17}\text{O}$	$\frac{5}{2}_1^+$	0.0	-0.7652 [57]	-0.54	-0.75752(4) [95]	+0.471
${}^{21}\text{Ne}$	$\frac{3}{2}_1^+$	0.0	-0.500 [57]	—	-0.441198(3) [96]	+0.476
	$\frac{5}{2}_1^+$	0.351	-0.230 [57]	-0.54	-0.196(12) [97]	+0.476
${}^{25}\text{Mg}$	$\frac{5}{2}_1^+$	0.0	-0.340 [57]	-0.54	-0.34218(3) [98]	+0.480
${}^{29}\text{Si}$	$\frac{1}{2}_1^+$	0.0	-1.114 [57]	-2.67	-1.1106(6) [99]	+0.483
${}^{33}\text{S}$	$\frac{3}{2}_1^+$	0.0	+0.387 [100]	+0.54	+0.4292141(9) [101]	+0.485
${}^{37}\text{Ar}$	$\frac{3}{2}_1^+$	0.0	+0.601 [102]	+0.54	+0.763(3) [103]	+0.486
	$\frac{7}{2}_1^-$	1.611	-0.43 [104]	-0.38	-0.38(2) [105]	+0.486
${}^{41}\text{Ca}$	$\frac{7}{2}_1^-$	0.0	-0.49 [53]	-0.38	-0.455652(3) [106]	+0.488
${}^{45}\text{Ti}$	$\frac{7}{2}_1^-$	0.0	+0.159 [107]	-0.38	+0.027(1) [108]	+0.489
	$\frac{5}{2}_1^-$	0.0393	-0.292 [107]	+0.38	-0.053(4) [109]	+0.489

Table 2: Nuclear g-factors for the ground and excited states of the lightest $N = Z + 1$ nuclei, replacing the α -cluster values in tab. 1 by the Schmidt estimates (SE). The negative sign of the reported values reflects convincingly the negative magnetic moment of the added neutron. In contrast with tab. 1, the ratios Z/A do not agree with the experimental g-factors.

Concerning ${}^{17}\text{O}$, attempts to reproduce the spectrum of the nucleus above the ${}^{13}\text{C}+\alpha$ decay threshold in terms of the $4\alpha + n$ configuration have been made [84, 85] in the framework of the generator coordinate method (GCM) [86]. Nevertheless, for the lowest-energy states, SM-based approaches as the cluster-orbital shell model (COSM) [87] seem to provide a rather faithful description [88, 89]. Moreover, a recent CSM analysis of the whole low-energy spectrum and the electromagnetic multipole transition probabilities of ${}^{21}\text{Ne}$ [42] suggests, that particle and hole neutron states can coexist with the underlying ${}^{20}\text{Ne}$ core, thus exciting the internal degrees of freedom of one of the α -particles. The comparison with the experimental energies turns out to be favourable for the model, except for the missing $K^P = 1/2^+$ band starting at 17.34 MeV [42]. Besides, the g-factor of the $(3/2)_1^+$ state, inferred from the magnetic moment [42] with the free

value for g_s^n , is equal to -0.287 , *i.e.* smaller in magnitude than the experimental one in tab. 2. The value is obtained by addition of the g-factor of the 5α bi-pyramidal core (cf. eq. (3)) with the contribution of the unpaired neutron, $-0.85 \mu_N$, times suitable Clebsch-Gordan coefficients (cf. eq. (20) in ref. [42]).

Switching to heavier nuclei, the cross section of elastic and inelastic scattering of α -particles suggests that α -particles at least at the surface level are present and interact with the incoming α -particle [90]. Moreover, in ^{41}Ca and ^{45}Ti , α -clusters can be induced by the pairing interaction alone at large values of the strength parameter G or at physical values of the latter, provided a four-nucleon force is introduced in the Hamiltonian [90].

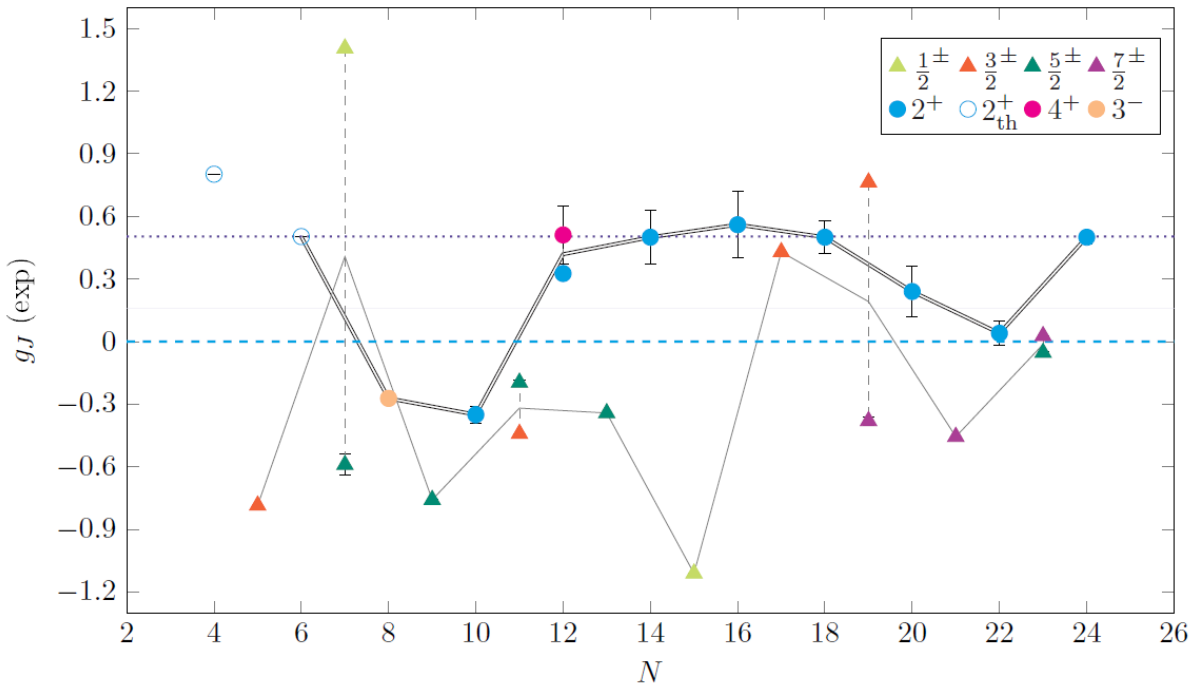


Figure 2: Behaviour of the experimental g-factor values as a function of the neutron number for ground and excited states of odd nuclei with $N = Z + 1$ (triangles) and even-even nuclei with $N = Z + 2$ (circles). The theoretical values available for ^{10}Be and ^{10}C are denoted with an open circle. The double (single) line joins the averaged values of the g-factors for the ground and excited states (when present) related to the $N = Z + 2$ ($N = Z + 1$) nuclei.

The experimental data of the gyromagnetic factors for this class of nuclei (cf. tab. 2) highlight large deviations from the α -cluster value in eq. (4), as a result of the significant spin contribution from the unpaired neutron. The fact itself that the magnetic moment is not parallel to the total angular momentum leads to strongly J-dependent values of the g-factor in excited states of the same nucleus. Exemplary is the case of the $(1/2)_1^-$ and the $(5/2)_1^+$ states of ^{13}C (cf. fig. 2), whose g-factors differ by almost two units and the sign.

As a consequence, we replace the macroscopic α -cluster result in eq. (3) by the Schmidt formula [39], that attaches the magnetic moment to the unpaired nucleon,

$$\boldsymbol{\mu} = \frac{e}{2m_u} (g_\ell^u \boldsymbol{\ell} + g_s^u \mathbf{s}) , \quad (7)$$

where $u = n$ or p . Due to the inequality between the orbital and the spin gyromagnetic factors, $\boldsymbol{\mu}$ precesses about the angular momentum $\mathbf{j} = \boldsymbol{\ell} + \mathbf{s}$ of the single-particle ground or excited state. The reported values of the nuclear g-factors are extracted from the magnetic moments by taking the projection of $\boldsymbol{\mu}$ on the total angular momentum operator of the nucleus, \mathbf{J} ,

$$\boldsymbol{\mu}_J \equiv \frac{e}{2m_u} g_J \mathbf{J} = \frac{\mathbf{J} \cdot (g_\ell^u \boldsymbol{\ell} + g_s^u \mathbf{s})}{J(J+1)\hbar^2} \frac{e\mathbf{J}}{2m_u}, \quad (8)$$

where \mathbf{J} is assumed to coincide with the one of the single-particle state \mathbf{j} and the inner products are evaluated via the Landé formulae,

$$\boldsymbol{\ell} \cdot \mathbf{J} = \frac{\hbar^2}{2} [J(J+1) + \ell(\ell+1) - s(s+1)], \quad (9)$$

$$\mathbf{s} \cdot \mathbf{J} = \frac{\hbar^2}{2} [J(J+1) + s(s+1) - \ell(\ell+1)]. \quad (10)$$

The description of $\boldsymbol{\mu}$, merely in terms of the unpaired particle, proved to be quite effective for nuclei in the vicinity of a closed shell [110]. In addition, the adoption of quenched values for g_s^p and g_s^n in the Schmidt estimates for the gyromagnetic factors permits to improve the estimates for the open-shell nuclei, at the price of deteriorating slightly the good agreement with the experimental values of the ^{17}O and ^{41}Ca nuclei (cf. tab. 2 and fig. 2).

In fact, the Schmidt estimates for the sd -shell nuclei improve and quite accurate predictions are obtained for the $(5/2)_1^+$ state of ^{25}Mg , as well as for the $(3/2)_1^+$ one of ^{33}S and the $(3/2)_1^+$ and $(7/2)_1^-$ of ^{37}Ar . Conversely, the values of $g^{(SE)}$ associated with the $(7/2)_1^-$ ground state and the $(5/2)_1^-$ excited state of ^{45}Ti , sharply disagree with the experimental data. It follows that a larger model space is required for this nucleus, lying in the pf -shell, in order to obtain order-of-magnitude agreement with the observed g-factors. The small excitation energy of the $(5/2)_1^-$ state itself is an indicator of *collective motion*.

Concerning the shell-model estimates for ^9Be , calculations with phenomenological interactions encompassing the active nucleons in the p -shell ($0 \hbar\omega$ space) as well as the excitations to the sd -shell ($1 \hbar\omega$ space) produce a g-factor for the $(3/2)_1^-$ state differing by less than 10% from the experimental counterpart [91]. The deviation reduces to nearly 1 % in the microscopic $2\alpha + n$ model in ref. [111], where $g \approx -0.779$, thus lending further weight to the *molecular* treatment of the unpaired nucleon moving around the α -clusters.

For ^{13}C , the former shell-model calculation with phenomenological interaction yields a similar agreement with the experimental g-factor of the ground state, whereas a more recent one based on Warburton-Brown interactions underestimates the same g-factor by 10 % [112]. The closest available estimate to the measured g-factor in tab. 2 yields +0.707 [113] and is based on the ^4He core in the p - sd model space and with $2 - 3 \hbar\omega$ excitations, adopting the bare values of the proton and neutron g-factors. The result for the $(5/2)_1^+$ excited state turns out to be even closer to the experimental value, which is indeed well reproduced ($g \approx -0.62$) by the minimal coupling model in ref. [114], that assumes a self-conjugate ^{12}C core.

On the other hand, the g-factors of the sd -shell nuclei up to ^{29}Si are obtained from USDB interaction [65], and some disagreement with the experimental data is detected only for the $(3/2)_1^+$ and $(5/2)_1^+$ states of ^{21}Ne [57]. The discrepancy is slightly filled by the ab-initio in-medium similarity renormalization group (IM-SRG) approach, yielding $g = -0.443$ and -0.140 for the two states, respectively.

Concerning the $(3/2)_1^+$ of ^{33}S , the sd -shell model calculation in ref. [100] with the empirical Hamiltonian of ref. [66] reproduces the experimental g-factor within less than 10 % deviation. Moreover, the gyromagnetic factor of the Schmidt estimate approaches the measured value, thus suggesting that the largest contribution comes from the odd neutron in the $d_{3/2}$ shell [100].

Assuming a ^{28}Si core with configuration mixing and effective g_s^p and g_s^n for the $1s_{1/2}$ and $0d_{3/2}$ shells, the g-factor of the analogous $(3/2)_1^+$ state of ^{37}Ar has been computed in ref. [102], when the experimental counterpart was unavailable. From the different shell-model estimates for the magnetic dipole moments of tab. 1 in ref. [102] follows, that a better agreement with the observed value of this state is obtained when the g-factors of the free nucleons are adopted [102]. For the $(7/2)_1^+$ state of the same nucleus, in tab. 2 the shell-model state with negative parity is constructed from a ^{36}Ar core with a single neutron in the pf -shell, exploiting the free nucleon g-factors [104]. Core polarization effects are included in the calculation, by considering both the 0_1^+ and the 1^+ levels of the α -conjugate core. The resulting g-factor is compatible within four standard deviations with the experimental value.

In the ^{41}Ca case, the reference result arises from a large scale sd - pf shell-model calculation with ^{28}Si core and USD [67], and modified Kuo-Brown [115] interactions for the sd and pf shells, respectively, and LKS [116] interaction for the mixing of the two major shells. The g-factor in tab. 2 is found to reproduce with less than 10% deviation the experimental value, even if the free values for g_s^p and g_s^n are employed.

Finally, the gyromagnetic factors of the $(7/2)_1^-$ and $(5/2)_1^-$ states of ^{45}Ti are drawn from the shell model calculation in the pf model space with phenomenological interactions in ref. [107], in which g_s^p and g_s^n in the pf shell are fitted to reproduce the experimental magnetic moment of the ground state of ^{41}Ca (and ^{41}Sc). The g-factors of the two levels of ^{45}Ti in tab. 2 turn out to be overestimated in magnitude, although less than the Schmidt estimates, but possess the correct sign. Nevertheless, the application of the Nilsson model in ref. [117] with oblate deformation yields a g-factor of -0.003 for the $7/2^-$ ground state [117], underestimated but sensibly closer to the measured counterpart.

2.3. $N = Z + 2$ nuclei

In the following, we add another neutron to the original even-even self-conjugate nuclei and investigate, how the two extra neutrons affect the inner α -cluster structure.

As in ^9Be case, for the ^{10}Be nucleus, a number of studies examining the low-lying spectrum and the reduced electric and magnetic transition probabilities exists in microscopic or semi-microscopic

pictures. Among these, the LCAO [118] and the antisymmetrized molecular dynamics (AMD) [119] have established that α -clustering in ^{10}Be emerges already in the ground and excited states of the $K^P = 0^+$ band, where the two valence neutrons form structures equivalent to π bonds. The separation between the ^4He clusters grows in the second $K^P = 0^+$ and in the negative parity band $K^P = 1^-$, where the two neutrons give rise to σ -like molecular bonds [119].

NUCLEUS	LEVEL	ENERGY [MeV]	$g^{(SM)}$	$g^{(SE)}$	$g^{(exp)}$	Z/A
^{10}Be	2_1^+	3.368	+0.503 [126, 127]	-0.45	—	+0.400
^{10}C	2_1^+	3.354	+0.802 [126]	+1.99	—	+0.600
^{14}C	3_1^-	6.728	-0.261 [128]	-0.30	-0.272(7) [128]	+0.429
^{18}O	2_1^+	1.982	-0.3995 [57]	-0.20	-0.35(4) [33]	+0.444
^{22}Ne	2_1^+	1.982	+0.374 [57]	-0.19	+0.326(12) [72]	+0.455
	4_1^+	3.357	+0.511 [57]	-0.14	+0.55(14) [72]	
^{26}Mg	2_1^+	1.809	+0.8695 [57]	-0.19	+0.50(13) [129]	+0.462
^{30}Si	2_1^+	2.235	+0.366 [57]	-0.27	+0.56(16) [130]	+0.467
^{34}S	2_1^+	2.128	+0.50 [76]	-0.27	+0.50(8) [131]	+0.471
^{38}Ar	2_1^+	2.167	+0.309 [64]	-0.84	+0.24(12) [64]	+0.474
^{42}Ca	2_1^+	1.525	+0.13 [132]	-0.13	+0.04(6) [132]	+0.476
^{46}Ti	2_1^+	0.889	+0.285 [133]	-0.13	+0.50(3) [133]	+0.478

Table 3: Nuclear g-factors for excited states of $N = Z + 2$ nuclei, including ^{10}C . As noticed in tab. 2, the ratios Z/A do not follow with the measured g-factors.

Moreover, the application of the AMD in combination of the GCM in ref. [120] unveiled that the 0_1^+ , the 2_1^+ and the 3_1^- states of ^{14}C possess intermediate features between a triaxial α -clustered configuration and a SM state, in which the two neutrons lie in the closed p -shell, while the protons fill the $p_{3/2}$ level. On the other hand, the 0_2^+ , 2_2^+ and 4_1^+ have a significant overlap with a triangular α -cluster configuration, in which the two neutrons stand in the same plane of the ^4He clusters and fill two sd -like orbitals [120]. Linear-chain α -cluster states are, indeed, found to characterize the 0_5^+ , 2_6^+ and 4_6^+ states located in the vicinity of the $\alpha + ^{10}\text{Be}$ decay threshold [120].

Concerning ^{18}O , the levels 0_1^+ , 2_1^+ and 4_1^+ below the $^{14}\text{C} + \alpha$ threshold in the GCM model in ref. [121] have a strong overlap with the SM $0 \hbar\omega$ prolate or spherical configuration, whereas the states belonging to the second $K^P = 0^+$ band support the formation of the inner $\alpha + ^{14}\text{C}$ structure [121].

A similar study [122] conducted on ^{22}Ne predicts the existence of a $K^P = 0^+$ α -clustered band as well as negative parity doublets located above the $^{18}\text{O} + \alpha$ threshold. Although less abundant, some theoretical cluster studies for the heavier α -conjugate nuclei are available, such as the ones in the framework of the weak coupling approach of the α -particle (or hole) with respect to a ^{40}Ca core [123], or in the semi-microscopic algebraic cluster model (SACM) [124, 125]. The existence of

parity doublet bands with $K^P = 0^+$ and 0^- in the neighbourhood of the lowest α -decay threshold is considered as a signature for the decomposition of the nucleus into a core plus an α -particle [123].

Regarding the g-factors of excited energy levels, their values are evidently correlated to the shell-closures. In particular, from the behaviour of the double lines in fig. 2, we infer that in the semi-magic nuclei at the $N = 8$ (resp. 20) shell closures, namely ^{14}C and ^{18}O (resp. ^{38}Ar and ^{42}Ca) the effect of the two extra neutrons is maximum (cf. tab. 3). For these nuclei, single-particle estimates are expected to reproduce quite accurately the g-factors, even when the free values of g_s^p and g_s^n are adopted.

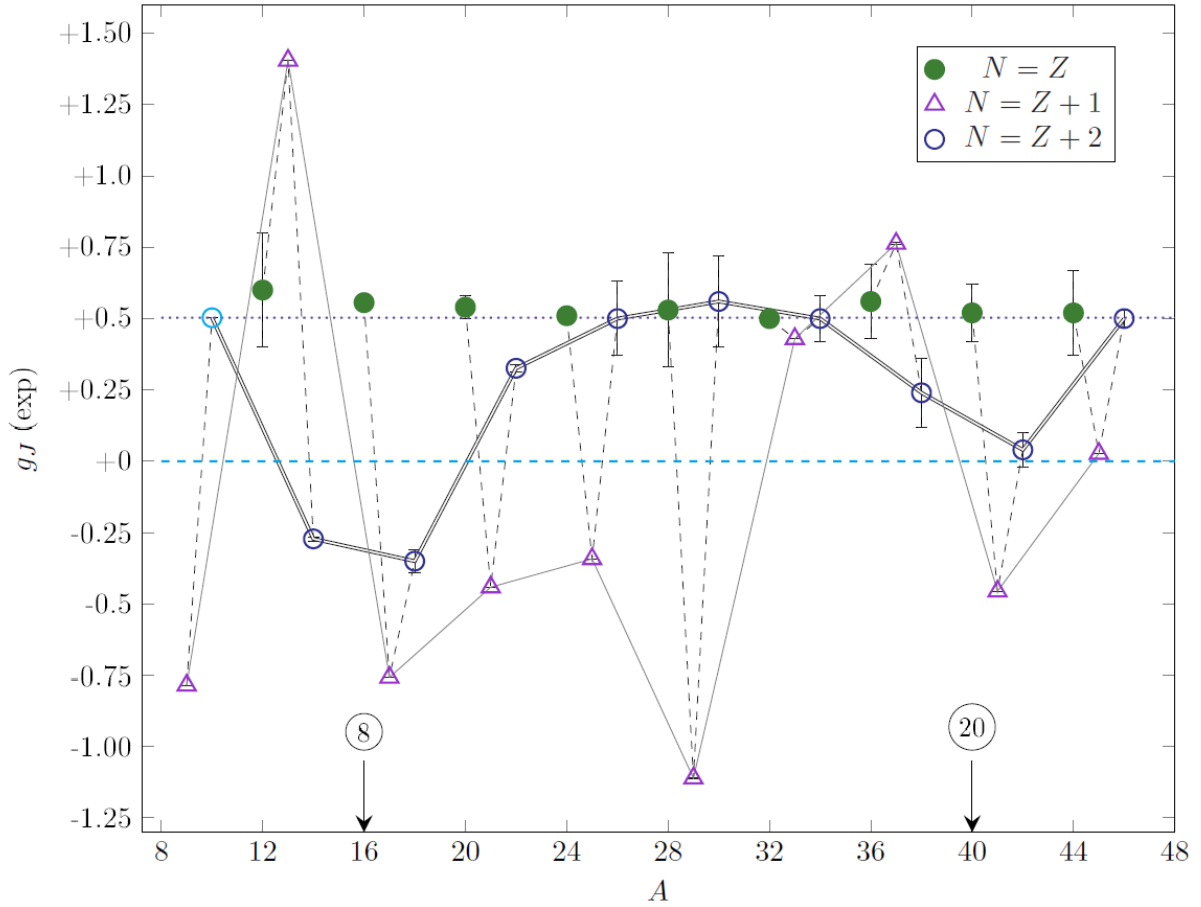


Figure 3: Behaviour of the experimental g-factor values as a function of the mass number for ground and/or excited states of α -conjugate nuclei (full circles), odd nuclei with $N = Z + 1$ (open triangles) and even-even nuclei with $N = Z + 2$ (open circles). The dotted line at $g_J \approx 0.5034$ denotes the gyromagnetic factor predicted by macroscopic α -cluster models. The theoretical value available for ^{10}Be is depicted in a lighter shade. The shell closures at $N, Z = 8$ and 20 are marked by arrows. Gyromagnetic factors referring to isotopes of the same nucleus are connected by dashed lines. The double (single) lines join the averaged values of the g-factors for the ground and excited states (when present) related to the $N = Z + 2$ ($N = Z + 1$) nuclei.

For the other nuclei, located before, between or beyond the two shell closures (cf. tab. 3), no significant discrepancy is found with respect to the macroscopic α -cluster prediction, with the sole exception of the g-factor of the 2_1^+ state of ^{22}Ne . For all other nuclei, the experimental g-factors

agree within one standard deviation with $\approx +0.5034$. Additionally, for the 4_1^+ state of ^{22}Ne , the g-factor turns out to be again compatible with the prediction of eq. (4). Since the pairing force couples equal nucleons with opposite total angular momentum projection, this interaction is not responsible for the suppression of the isovector contribution to the g-factor. On the other hand, four-body correlations between pairs of equal nucleons can quench $g_J^{(1)}$ and reduce the $g_J^{(0)}$ to $1/2$, due to the vanishing total spin.

The application of AMD + GCM in ref. [120] to the low-lying states of ^{14}C , suggests that the considered 3_1^- level in tab. 2 has a spatial distribution, intermediate between a SM state with the protons in the $p_{3/2}$ subshell and the neutrons in the $1p-1h$ excited configuration and a triangular α -cluster state. In fact, the single-particle Gaussian wave-packets of the two neutrons gather still around the origin [120], despite a slight overall triaxial deformation ($\beta \approx 0.22$, $\gamma \approx 24^\circ$). Also, the GCM analysis in ref. [121] predicts a strong overlap with a SM state for the 2_1^+ state of ^{18}O in tab. 3. We can deduce that, when the wavefunctions of the two extra neutrons overlap significantly in the space, clustering is hindered [134] and the g-factor displays significant deviations from eq. (4). Otherwise, if the two neutrons are spatially more separated, *e.g.* when sitting between two different pairs of α -particles in the molecular picture [134], the g-factor approaches the value of ≈ 0.5034 , as in α -conjugate nuclei.

Therefore, we can predict that at higher-lying energy levels of ^{14}C and ^{18}O such as the 2_2^+ state, where clustering is expected to be more pronounced [121, 120], the g-factor reaches the one of the other levels of the open-shell even-even $N = Z + 2$ nuclei in tab. 3. The shell closures at $N = 8$ and 20 (cf. fig. 3), in fact, seem to favour a more compact spatial distribution of the two neutrons, that undermines α -clustering in the low-lying energy states of the nearby semi-magic nuclei, (cf. ^{14}C , ^{18}O , ^{38}Ar and ^{42}Ca in tab. 3).

Although of a milder type, the phenomenon takes place also in the two considered states of ^{22}Ne , where the measured g-factor of the 2_1^+ state differs by 35 % with respect to the macroscopic α -cluster value.

As in the previous section, we give the shell-model g-factors in tab. 2 and the Schmidt estimates, that we obtain through the quenched values of g_s^p and g_s^n . The g-factor of the excited states of this class of nuclei is now attributed to two neutrons lying on two distinct single-particle states with angular momentum \mathbf{j}_1 and \mathbf{j}_2 , which sums up to \mathbf{J} .

Next, the g-factors corresponding to the two single-particle levels are combined together, giving the overall g_J factor through the formula

$$g_J = \frac{g_1 \mathbf{j}_1 + g_2 \mathbf{j}_2}{J(J+1)\hbar^2} \cdot \mathbf{J} = \frac{1}{2}(g_1 + g_2) + \frac{1}{2} \frac{j_1(j_1+1) - j_2(j_2+1)}{J(J+1)}(g_1 - g_2). \quad (11)$$

Applying eq. (11) we obtain the values of the g-factors reported in the $g^{(SE)}$ column of tab. 3. As it can be observed, the Schmidt estimates for the listed levels of ^{14}C , ^{18}O and ^{42}Ca at the chosen value of g_s^n prove to be quite predictive, whereas for the 2_1^+ state of ^{22}Ne , ^{26}Mg , ^{30}Si , ^{34}S , ^{38}Ar and ^{46}Ti large discrepancies, including the sign, are found with the experimental values. This fact highlights the sensitivity of the magnetic dipole moment to shell-closure effects in semi-magic

nuclei as ^{14}C , ^{18}O and ^{42}Ca , where the g-factors are determined by either the two extra neutrons or the two missing protons.

Concerning the SM estimates, the gyromagnetic factor of the 2_1^+ state of ^{10}Be , calculated via the Monte Carlo shell-model (MCSM) with nucleon-nucleon interactions drawn from Chiral Effective Field Theory in the unitary correlation operator method (UCOM) [135, 136], turns out to reproduce faithfully the value of eq. (4), thus suggesting a well-developed α -cluster structure, with the two neutrons acting as valence particles in a π orbital of a binary molecule (cf. ref. [119]). Although ^{10}Be is a rather long-lived isotope, the magnetic moments associated with its excited states have not yet been measured.

For ^{14}C , the SM calculation, reported in ref. [128], is based on a ^{16}O core with three holes in the p -shell and one particle in the sd -shell. Besides, for the nucleons in the p -shell, the Cohen-Kurath two-body matrix elements [83] are adopted, whereas the Gillet interaction [137] is exploited between the p and sd -shell nucleons. The result is closer in magnitude with respect to the more recent estimate in ref. [112], obtained with the phenomenological V_{MU} , SFO and SDPF-M interactions.

The data obtained from the phenomenological USDB interaction [65] for the sd -shell (cf. tab. I in ref. [57]) permit to reproduce quite accurately the g-factors of the 2_1^+ state of ^{18}O as well as the 2_1^+ and 4_1^+ states of ^{22}Ne , assuming the free value of g_s^p (g_s^n) and an effective charge of $e_p = 1.5e$ ($e_n = 0.5e$) for the protons (neutrons). In contrast, for the 2_1^+ state of ^{26}Mg and ^{30}Si , less agreement with the central values of the experimental data is attained [57]. In both cases, a more satisfactory answer is provided by the IM-SRG approach, that yields $g = +0.512$ and $g = +0.420$ for the two nuclides, respectively [57], both more compatible with the experimental values.

Regarding ^{34}S , the g-factor obtained in the large-scale SM calculation with sd - pf configuration mixing in ref. [76] is in excellent agreement with the observed result, whose central value is the closest to the macroscopic α -cluster value and its statistical error is smaller than for the neighbouring nuclei in tab. 3. The mixing between the sd and pf major shells has not been considered in the ^{38}Ar case, where the g-factor of the 2_1^+ is obtained entirely from the sd model space with the Warburton-Brown interactions [68], but with the same convention for the nucleon charges as well as for g_s^n and g_s^p . The result is still compatible with the experimental g-factor (cf. tab. 3).

The large-scale sd - pf SM calculation in ref. [132] produces a compatible value for the g-factor of the 2_1^+ state of ^{42}Ca , which the Schmidt estimate in tab. 3 reproduces with the same magnitude but opposite sign. Underpinning this calculation is the enlarged model space, that assumes the α -conjugate nucleus ^{28}Si as a core and the USD interactions [67] in the sd -shell, the modified Kuo-Brown ones [115] in the pf -shell and the LKS potentials [116] between the two major shells. The ^{40}Ca core excitations are found to provide substantial improvement with respect to the pf -shell estimates reported in ref. [132], thus indicating a deviation from sphericity in the ^{40}Ca core. Eventually, the pf -shell model (FSM) calculation in ref. [133] with modified Kuo-Brown (KB3) interactions [115] sensibly underestimates the g-factor of the lowest 2^+ state of ^{46}Ti , as a result

of the limited size of the model space. In ^{45}Ti (^{46}Ti), the smallness of the excitation energy of the $7/2_1^-$ (2_1^+) state suggests an underlying *collective* nature. Hence, a larger number of valence nucleons in the SM calculation or an α -clustered ^{44}Ti core would be recommendable.

3. The ^{12}C nucleus

Here, we present the theoretical predictions for the magnetic dipole moment of two energy levels of the ^{12}C nucleus within a macroscopic α -cluster model. For the latter, we select the Hamiltonian with the α - α interaction given by the isotropic Ali-Bodmer [138] potential in ref. [43] with the same parameters as in sec. II A of ref. [44]. On top of the latter, reproducing the short-range repulsive and long-range attractive effects of the strong force (cf. eqs. (2) and (3) of ref. [46]), we add the Coulomb interaction, accounting for the spherical charge distribution of the ^4He nucleus with charge radius $R_\alpha = 1.44$ fm (cf. eq. (4) of ref. [46]), as well as the Gaussian 3α force (cf. eq. (5) of ref. [46]), whose strength and range parameters were originally fitted to reproduce the binding energy of ^{12}C and the $2_1^+ - 0_2^+$ energy difference respectively (cf. refs. [139, 43]). However, due to the adopted isotropic Ali-Bodmer potential with the parameters given in ref. [44], the energy of the ground state of this nucleus coincides with the opposite of the Hoyle state gap in the continuum and infinite-volume limit.

As in refs. [44, 46], we transpose the above system of α -particles in a finite cubic lattice of side $L = Na$ with N points per dimension, with a the lattice spacing. To the wavefunctions of the lattice Hamiltonian (cf. sec. 3.1 and 3.2 of ref. [46]), we impose periodic boundary conditions (PBCs). As a consequence, the M -body relative configuration space in the continuum and infinite volume, \mathbb{R}^{3M-3} , is reduced to a torus in $3M-3$ dimensions. This operation produces manifold implications in the Hamiltonian and its eigenfunctions, the most glaring of them is rotational symmetry breaking, represented by the descent in the symmetry from $\text{SO}(3)$ to the cubic group, $\text{SO}(3, \mathbb{Z})$ [44, 45] or \mathcal{O} [46, 140], consisting of the 24 rotations of the regular hexahedron.

The latter and the other discrete symmetries of the lattice Hamiltonian, outlined in sec. 4 of ref. [46], permit to classify the lattice eigenstates in terms of the irreducible representations of parity, \mathcal{O} and the group of the permutation of M particles. Taking the bosonic nature of α -particles into account, we consider only the completely symmetric representation of the latter group,

$$\square\square\dots\square = [M] \equiv S, \quad (12)$$

and apply the associated projectors in the numerical procedure for the extraction of the lattice eigenstates (cf. sec. 6 of ref. [46]). As in refs. [44, 46], we introduce the lattice counterpart of $\text{SO}(2)$, i.e. the cyclic group of order four, \mathcal{C}_4 , associated to the counterclockwise rotation of $\pi/2$ about the z axis. Labeling the irreps of the former, I_z , by positive integers modulo 4 [44], and identifying the irreps of the cubic group with Γ [46], we represent each lattice eigenstate with a round bracket (cf. ref. [45]) as

$$|\mathcal{N}, \Gamma, I_z, S, \mathcal{P}\rangle, \quad (13)$$

where \mathcal{N} is a positive nonzero integer that denotes the order with which the lattice eigenstates with the same transformation properties appear in the spectrum, thus fulfilling the role of the principal quantum number. When the $\text{SO}(3)$ multiplet to which each state belongs in the continuum and infinite volume is identified, the angular momentum quantum number, ℓ , is added to the lattice states. Starting from states with well-defined I_z (cf. eq. (13)) and part of the same $\text{SO}(3)$ multiplet, it is possible to obtain states with good angular momentum projection along the z-axis in the continuum and infinite volume limit. The replacement of the \mathcal{C}_4 by the $\text{SO}(2)$ label is performed through the unitary transformation discussed in app. C of ref. [140] and presented for completeness in the tabs. ??-17 for $\ell \leq 9$ in the appendix. In this transformed basis, the lattice eigenstates become

$$|\mathcal{N}, \ell, m, S, \mathcal{P}\rangle, \quad (14)$$

where the label Γ has been dropped for brevity.

Exactly the states in eq. (14) constitute the main ingredient for the computation of the average values of the magnetic dipole moment operator (cf. [110]), defined in the relative reference frame as

$$\begin{aligned} \mu(\mathcal{N}, \ell, \mathcal{P})^{(r)} &\equiv (\mathcal{N} \ell \ell S \mathcal{P} | \hat{\mu}_0^{(r)} | \mathcal{N} \ell \ell S \mathcal{P}) \\ &= (\mathcal{N} \ell \ell S \mathcal{P} | \mu_N g_L^{(\alpha)} \sum_{i=1}^{M-1} \frac{(\mathcal{L}_{iM})_z}{\hbar} | \mathcal{N} \ell \ell S \mathcal{P}) \end{aligned} \quad (15)$$

where $g_L^{(\alpha)}$ is given by eq. (4) and $(\mathcal{L}_{iM})_z$ is the z-component of the angular momentum operator on the lattice. Its expression, consistently with the formula of the squared total angular momentum derived in sec. 3.3 of ref. [46], is defined in the relative frame by

$$(\mathcal{L}_{iM})_z = a\hbar \sum_{\mathbf{n}_i \in \mathcal{N}} \sum_{k=1}^K C_k^{(1,K)}(\mathbf{n}_{iM})_x \left[a_{iM}^\dagger(\mathbf{n}_{iM} + k\mathbf{e}_y) a_{iM}(\mathbf{n}_{iM}) - a_{iM}^\dagger(\mathbf{n}_{iM} - k\mathbf{e}_y) a_{iM}(\mathbf{n}_{iM}) \right], \quad (16)$$

where $a_{iM}^\dagger(\mathbf{n}_{iM})$ and $a_{iM}(\mathbf{n}_{iM})$ are the creation and annihilation operators of the α -particle i relative to the α -particle M at the site (\mathbf{n}_{iM}) of the lattice, whereas the coefficients $C_k^{(1,K)}$, that scale as the inverse of the lattice spacing, are defined in refs. [46, 140]. Considering the fact that the center-of-mass degrees of freedom have been dropped from the Hamiltonian, the l.h.s. of eq. (15) is equivalent to the magnetic dipole moment in the absolute reference frame,

$$\begin{aligned} \mu(\mathcal{N}, \ell, \mathcal{P})^{(a)} &\equiv (\mathcal{N} \ell \ell S \mathcal{P} | \hat{\mu}_0^{(a)} | \mathcal{N} \ell \ell S \mathcal{P}) \\ &= (\mathcal{N} \ell \ell S \mathcal{P} | \mu_N g_L^{(\alpha)} \sum_{i=1}^M \frac{(\mathcal{L}_i)_z}{\hbar} | \mathcal{N} \ell \ell S \mathcal{P}), \end{aligned} \quad (17)$$

where the coordinate of the M^{th} particle is extracted from the relative ones of the other particles, subject to the constraint that $\mathbf{r}_{CM} = 0$.

Furthermore, the computation of the magnetic dipole moment associated with the two energy levels, provides the opportunity to continue the analysis of the artifacts induced by the lattice

environment in average values of spherical tensor operators that started in ref. [45]. In this respect, we here focus on the behaviour of the average values of the former observable with the lattice spacing and, aiming at reducing the discretization errors, we compute the *isotropic averages* (ref. [45]) of the magnetic dipole moments. Extending the definition in eq. (21) of ref. [45] to the magnetic dipole moment in the relative frame in eq. (15), the isotropically averaged expression of $\mu(\mathcal{N}, \ell, \mathcal{P})^{(r)}$ is obtained,

$$(\mathcal{N} \ell \ell S \mathcal{P} | \hat{\mu}_0^{(r)} | \mathcal{N} \ell \ell S \mathcal{P})_{\circ} = (\ell 1 \ell | \ell 0 \ell) \frac{1}{2\ell + 1} \sum_{m, m', m''} (\ell 1 \ell | m m' m'') \cdot (\mathcal{N} \ell m'' S \mathcal{P} | \mu_N g_L^{(\alpha)} \sum_{i=1}^{M-1} \frac{(\mathcal{L}_{iM})_{m'}}{\hbar} | \mathcal{N} \ell m S \mathcal{P})_{\circ}, \quad (18)$$

where the lattice angular momentum operator is expressed in the spherical basis and the Clebsch-Gordan coefficients of SO(3), $(\ell \ell' \ell'' | m m' m'')$, have been introduced in the notation of ref. [141].

The counterpart of the last equation in the absolute reference frame can be obtained by applying the same definition (cf. ref. [45]) to the matrix element $(\mathcal{N} \ell \ell S \mathcal{P} | \hat{\mu}_0^{(a)} | \mathcal{N} \ell \ell S \mathcal{P})_{\circ}$. Additionally, in the three sums over the SO(2) labels at the r.h.s. of eq. (18) only the projections m and m'' differing by zero or one unit of \hbar provide a nonzero contribution. To ponder the amount of each of the latter to the related isotropic average, it is convenient to define approximate reduced matrix elements, by resorting to the Wigner-Eckart theorem for SO(3) (cf. eq. (2.169) in ref. [141]). Applying the theorem, we define the reduced matrix elements of $\hat{\mu}$ between lattice eigenstates,

$$(\ell m || \hat{\mu}_{m'}^{(\rho)} || \ell m'') \equiv \frac{(\mathcal{N} \ell m S \mathcal{P} | \hat{\mu}_{m'}^{(\rho)} | \mathcal{N} \ell m'' S \mathcal{P})_{\circ}}{(\ell 1 \ell | m'' m' m)}, \quad (19)$$

in the relative and in the absolute reference frames, $\rho \equiv a$ or r . The definition in eq. (19) coincides with the one given in eqs. (15) and (19) of ref. [45], up to a factor equal to the Clebsch-Gordan coefficient $(\ell 1 \ell | 0 0 0)$ multiplied by the constant $\sqrt{3/4\pi}$.

As in the latter study, due to the breaking of rotational symmetry, the SO(2) labels have not been dropped in the definition of the reduced brackets in eq. (18). Additionally, we assume that the Clebsch-Gordan coefficients on the r.h.s. of eq. (19) do not vanish, a fact that is guaranteed by the triangular inequality between the angular momenta, $|\ell - 1| \leq \ell \leq \ell + 1$ and the conservation of the third component of the angular momentum $m' + m'' = m$. Besides, the latter three projections are also required to be nonzero, since the sum of the three angular momenta in eq. (19), $2\ell + 1$, is odd [141].

Reduced matrix elements can be immediately extended to the isotropic averages (cf. eq. (18)),

$$(\ell m || \hat{\mu}_{m'}^{(\rho)} || \ell m'')_{\circ} \equiv \frac{(\mathcal{N} \ell m S \mathcal{P} | \hat{\mu}_{m'}^{(\rho)} | \mathcal{N} \ell m'' S \mathcal{P})_{\circ}}{(\ell 1 \ell | m'' m' m)}, \quad (20)$$

with the same convention on the ρ index. Both the quantities in eqs. (19) and (20) are expected to reproduce asymptotically the exact reduced matrix elements in the continuum and infinite-volume

limit,

$$\langle \ell || \hat{\mu}^{(\rho)} || \ell \rangle \equiv \frac{\langle N \ell m S \mathcal{P} | \hat{\mu}_m^{(\rho)} | N \ell m'' S \mathcal{P} \rangle}{(\ell 1 \ell | m'' m' m)}, \quad (21)$$

where N is the counterpart of \mathcal{N} in the \mathbb{R}^{3M-3} configuration space.

Let us now begin with the behaviour of the magnetic dipole moment of the 2_1^+ state at 4.4398(2) MeV of ^{12}C as a function of the lattice spacing, displayed in fig. 4. As a result of the tuning of the parameters of the phenomenological 2α and 3α potentials of the present model [44, 46], in the continuum and infinite-volume limit the energy eigenvalue of this state converges to ≈ 3.35 MeV, as shown by the curves associated with the E and T_2 multiplets of the cubic group and by the corresponding multiplet-averaged (cf. eq. (50) of ref. [46]) solid line in figs. 28 and 32 in ref. [46]. By setting the side of the cubic lattice to $L \geq 19$ fm as in refs. [44, 46] we have reduced the finite-volume errors associated with the energy eigenvalues to $\approx 10^{-2}$ MeV, in order to remove the latter artifacts in the present analysis of discretization effects.

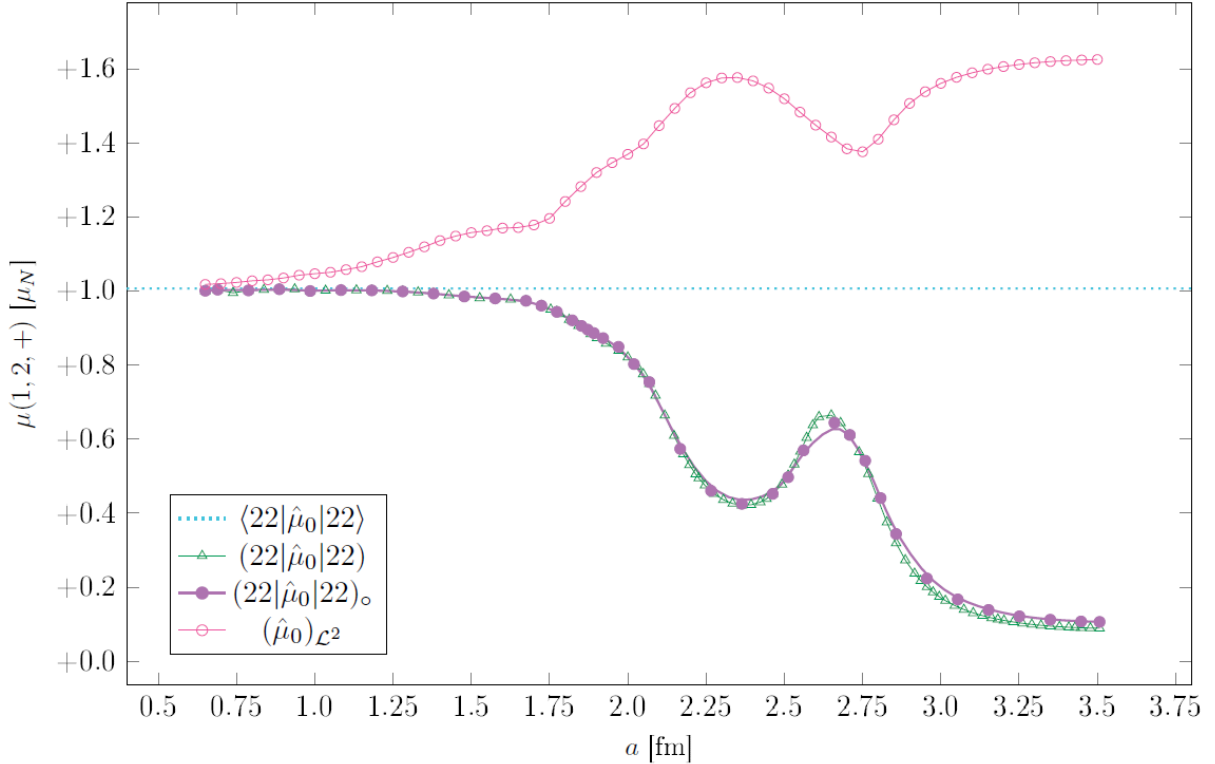


Figure 4: Average value of the magnetic dipole moment for the 2_1^+ energy level of ^{12}C as a function of the lattice spacing. The broken line with circles denotes the estimated magnetic dipole moments obtained from the multiplet-averaged values of the squared total angular momentum operator, \mathcal{L}^2 [46, 140], over the five wavefunctions composing the 2_1^+ level, degenerate in the continuum and infinite volume limit. The broken line with triangles denotes the matrix elements of the magnetic dipole moment operator (cf. eqs. (15) or (17)) over the lattice states with maximum projection along the z axis. The isotropically-averaged estimates of the same observable (cf. eq. (18)), extracted from the matrix element of $\hat{\mu}$ with lattice wavefunctions with a different third component of the total angular momentum operator, are displayed by the broken lines with squares. The theoretical value of $\approx +1.0068 \mu_N$ is marked with a dotted line and reproduced with 10^{-3} precision by the values of $\langle 22 | \hat{\mu}_0 | 22 \rangle$ and $(22 | \hat{\mu}_0 | 22)_o$ at $a \approx 0.65$ fm, both equal to $\approx 1.0018 \mu_N$. Finite-volume effects are suppressed by the constraint $Na \geq 19$ fm.

In its generality, the expression of the magnetic dipole moment operator for α conjugate nuclei in eq. (3) permits to obtain average values for $\hat{\mu}$ among states with maximum angular momentum projection, starting from estimates of the maximum \hat{L}_z eigenvalue. In the present case, the latter can be extracted from the average values of the squared total angular momentum operator as a function of the lattice spacing analyzed in fig. 39 of ref. [46]. Exploiting eq. (3) and the expression of the eigenvalues of \mathcal{L}^2 (cf. eqs. (24)-(27) of ref. [46]) in the continuum and infinite volume, $\ell(\ell+1)\hbar^2$, we have obtained the multiplet-averaged estimates of the magnetic dipole moments for the 2_1^+ state, that we denote with $(\hat{\mu}_0)_{\mathcal{L}^2}$. In fig. 4, the open circles at different values of the lattice spacing indeed describe a curve that lies always above the expectation value of the magnetic dipole moment at $+1.0068 \mu_N$, marked by a dotted line in fig. 4.

In particular, the minimum in $(\hat{\mu}_0)_{\mathcal{L}^2}$ at $a \approx 2.80$ fm corresponds to a deep minimum of the average value of \mathcal{L}^2 in the E multiplet of \mathcal{O} , constituting the 2_1^+ energy state in the continuum and infinite-volume limit (cf. fig. (39) of ref. [46]). In contrast to energy eigenvalues and the average values of the α - α separation (cf. \mathcal{E}_r and \mathcal{R} in figs. 32 and 33 of ref. [46]), the minima of the total squared angular momentum operator and hence $(\hat{\mu}_0)_{\mathcal{L}^2}$ cannot be unambiguously mapped to the local maxima of the probability density function associated to the lattice eigenstates they refer to. Concerning the isotropic average of the magnetic dipole moment (cf. eq. (18)), its behaviour with the lattice spacing shown by the curve with solid circles in fig. 4, follows quite faithfully the one of the magnetic dipole moment (open triangles in fig. 4) computed from the lattice 2_1^+ eigenstates with maximum angular momentum projection.

More precisely, $(22|\hat{\mu}_0|22)_o$ slightly quenches the discretization artifacts in the very large lattice spacing region ($a \gtrsim 2.75$ fm) as well as in a small region around $a \approx 2.37$ fm. However, for $a \lesssim 2.20$ fm no significant improvement in the estimate of the magnetic moment from the isotropic average is observed, whereas in the peak region around ($a \approx 2.60$ fm) the deviation from the asymptotic value of $\mu(1, 2, +)$ becomes even larger than for $(22|\hat{\mu}_0|22)$.

In summary, the isotropic average slightly reduces the discrepancies in the magnetic dipole moment between the extremal points. The reasons underlying this behaviour can be better understood by considering the individual reduced matrix elements (cf. eq. (19)) contributing to the reduced isotropic average in eq. (20). As it can be proven by rewriting the angular momentum operator in spherical components, the matrix elements contributing to the isotropic average in eq. (18) are overall 12 and fulfill the following symmetry relations:

$$(20||\hat{\mu}_0||20) = 0 ,$$

that vanishes as the associated Clebsch-Gordan coefficient, and

$$(22||\hat{\mu}_0||22) = -(2-2||\hat{\mu}_0||2-2) ,$$

$$(21||\hat{\mu}_0||21) = -(2-1||\hat{\mu}_0||2-1) ,$$

$$(20||\hat{\mu}_{-1}||21) = -(21||\hat{\mu}_1||20) = (2-1||\hat{\mu}_{-1}||20) = -(20||\hat{\mu}_1||2-1) ,$$

and

$$(2 - 1||\hat{\mu}_1||2 - 2) = -(2 - 2||\hat{\mu}_{-1}||2 - 1) = (22||\hat{\mu}_1||21) = -(21||\hat{\mu}_{-1}||22) . \quad (22)$$

Thanks to the identities in eq. (23), in fig. 5 we show the contributions of four reduced matrix elements to $(22||\hat{\mu}_1||22)_o$ in total. In particular, the elements $(20||\hat{\mu}_{-1}||21)$ and $(22||\hat{\mu}_0||22)$ display almost overlapping paths (cf. dashed lines with open pentagons and circles, respectively, in fig. 5), with slight deviations in the neighbourhood of $a \sim 2.05$ fm. Besides, these two contributions lie closest to the isotropic average and share the extrema with the latter, denoted by the solid curve with circles (cf. fig. 5).

Conversely, the dashed curve with open squares in fig. 5, that identifies the diagonal matrix element with intermediate angular momentum projection, displays overall the largest discrepancies from the isotropic average and exhibits a displaced local maximum at $a \approx 2.75$ fm, a fact does not uniquely depend on different the Clebsch-Gordan coefficients that multiply the various contributions to the isotropic average.

Similarly, the curve for the reduced matrix element $(21||r^2Y_2^0||21)$, associated with the electric quadrupole moment of the 2_1^+ state of ^8Be in fig. 2 of ref. [45]¹ displays the largest deviation in the shape and in the magnitude with respect to the relevant isotropic average (cf. the solid line with filled triangles in the latter figure). The same observation can be drawn from the matrix element $(21||r^4Y_4^0||21)$ for the electric hexadecupole moment of the same state of ^8Be in fig. 3 of ref. [45]. In the latter graph, also the contribution from the diagonal element with maximum angular momentum projection highlights large deviation from the isotropic average in magnitude, but the position of the extrema is closer to the one of the isotropic average than in the $(21||r^4Y_4^0||21)$ case.

Moreover, from fig. 5 it can be inferred that the curve of non-diagonal matrix element $(22||\hat{\mu}_1||21)$ follows a path intermediate between the one of the isotropic average and the $(21||\hat{\mu}_0||21)$ element, with a slightly shifted position of the local maximum.

Finally, from comparison between the magnetic dipole moment in the 2_1^+ of ^{12}C in fig. 5 and the quadrupole and hexadecupole electric moments in the 2_1^+ state of ^8Be in figs. 2 and 3 of ref. [45], we can conclude that the former observable is significantly less affected by discretization errors, in the same range of lattice spacing. More precisely, while all reduced matrix elements $(2m''||\hat{\mu}_{m'}||2m)$ at $a \approx 1.75$ fm differ by less than 10% to the continuum and infinite volume counterpart, at the same lattice spacing some of the contributions to the isotropically-averaged electric quadrupole and hexadecupole moment differ by more than 50 % from their respective asymptotic values.

Second, we consider the magnetic dipole moment of the 3_1^- state at 9.641(5) MeV of ^{12}C . In the adopted macroscopic α -cluster approach, the energy eigenvalue of the lattice counterpart of the 3_1^- state converges to ≈ 5.85 MeV above the *g.s.* in the continuum and infinite-volume limit (cf. fig. 36 of ref. [46]).

¹The matrix elements of the spherical tensor operators discussed in ref. [45] are expressed in unit of charge.

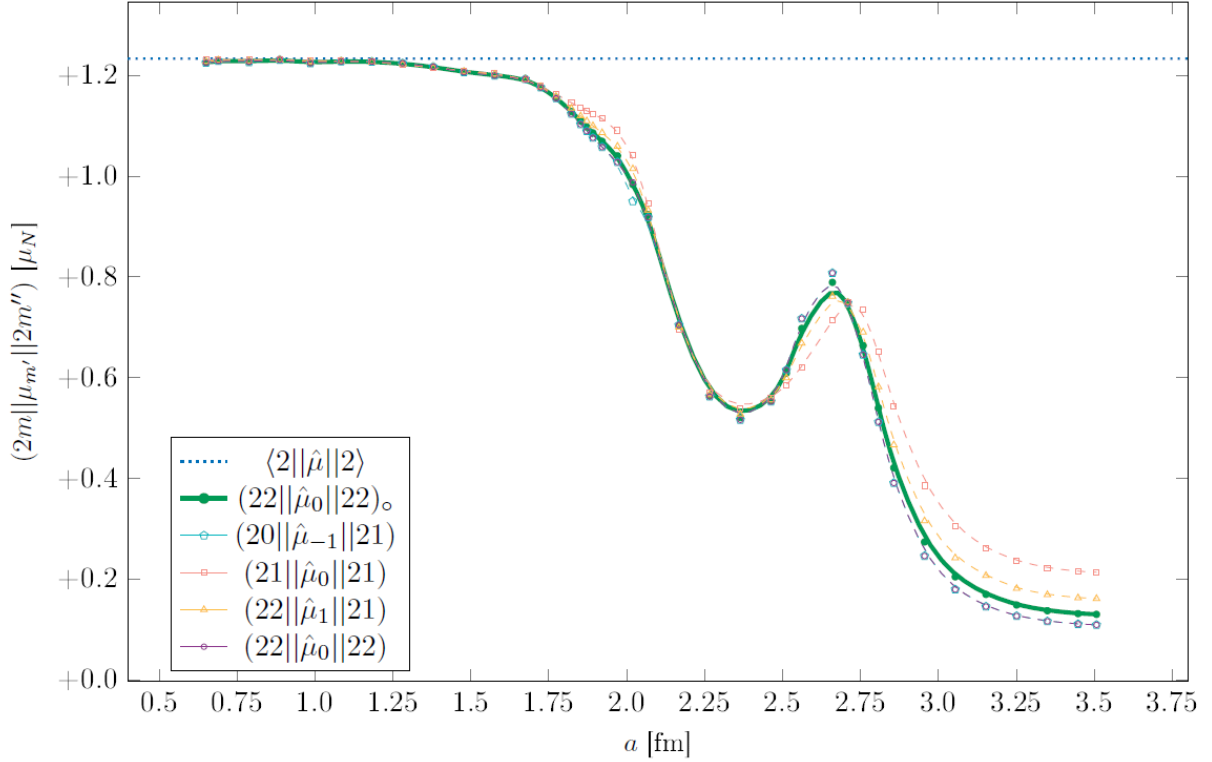


Figure 5: Behaviour of the reduced matrix elements between the spherical components of the magnetic dipole moment operator and lattice eigenstates with different angular momentum projection, m and m'' , along the z -axis as a function of the lattice spacing a for the 2_1^+ state of ^{12}C . The listed matrix elements represent the nonvanishing independent contributions to the isotropically-averaged estimate of the magnetic dipole moment in eq. (18), divided by the Clebsch-Gordan coefficient $(212|mm'm'')$. The asymptotic value of the reduced matrix elements in the continuum and infinite volume limit is represented by a dotted line and is independent of the third component of the angular momentum. The curves underlying each sample of matrix elements denote basis-spline functions calculated on the points of each dataset. In particular, the dashed (solid and thick) curve with open (filled) circles represents the reduced (isotropically-averaged) magnetic dipole moment. The diagonal matrix elements $(21||\hat{\mu}_0||21)$ with intermediate projection are denoted by a dashed curve with open squares, lying above all other curves in the large lattice spacing region. Finally, the behaviour of the off-diagonal matrix elements $(20||\hat{\mu}_{-1}||21)$ and $(22||\hat{\mu}_1||21)$ is described by the curves with open pentagons and triangles, respectively.

Starting from the multiplet-averaged value of the squared total angular momentum for the lowest A_2^- , T_1^- and T_2^- states (cf. fig. 40 of ref. [46]), an estimate of magnetic dipole moment can be obtained as for the 2_1^+ state. Fixing the lattice size $L \gtrsim 19.5$ fm, the corresponding magnetic moments, $(\hat{\mu}_0)_{\mathcal{L}^2}$, have been evaluated in an interval of lattice spacing ranging from 0.65 to 3.50 fm. As shown by the curve with open circles in fig. 6, these estimates lie above the expectation value of the magnetic moment (dotted line), with a minimum at $a \approx 2.80$ fm. The extremum is found in good correspondence with a sharp minimum in the average value of the squared angular momentum of the T_1 multiplet of states (cf. fig. 40 of ref. [46]).

Concerning the magnetic dipole moment computed from the state with maximum angular momentum projection along the z axis, $(33|\mu_0|33)$, the curve with open triangles in fig. 6 reaches the theoretical value of $\mu(1, 3, -)$ in the continuum limit from below and displays a minimum at

≈ 2.29 fm, as the curve for the 2_1^+ level of ^{12}C (cf. fig. 4). However, the decrease of $(33|\mu_0|33)$ in the region $1.75 \lesssim a \lesssim 2.25$ fm is steeper than the one of $(22|\mu_0|22)$ in the same interval (cf. fig. 4). Additionally, the discretization artifacts on $(33|\mu_0|33)$ at $a \gtrsim 1.75$ fm are significantly larger than for $(\hat{\mu}_0)_{\mathcal{L}^2}$, in contrast with fig. 4.

Nonetheless, the calculation of the isotropically-averaged value of $(33|\mu_0|33)$ (cf. eq. (18)) yields a sizable suppression of the discretization errors in the region $1.80 \lesssim a \lesssim 2.80$ fm, with a peak of $\sim 15\%$ around the local minimum at $a \approx 2.35$ fm. The curve for $(33|\mu_0|33)_o$, indeed, lies above the one for $(33|\mu_0|33)$ in the whole interval $0.65 \lesssim a \lesssim 3.10$ fm (cf. fig. 6), unlike the 2_1^+ case (cf. fig. 4). The origin of this behaviour can be better investigated by considering the individual contributions (cf. eq. (19)) to the reduced isotropic average in eq. (20). Specifically, the non-vanishing matrix elements on the r.h.s. of eq. (18) are now 18 and fulfill the following symmetry identities:

$$\begin{aligned} (30||\hat{\mu}_0||30) &= 0 , \\ (33||\hat{\mu}_0||33) &= -(3-3||\hat{\mu}_0||3-3) , \\ (32||\hat{\mu}_0||32) &= -(3-2||\hat{\mu}_0||3-2) , \\ (31||\hat{\mu}_0||31) &= -(3-1||\hat{\mu}_0||3-1) , \\ (30||\hat{\mu}_{-1}||31) &= -(31||\hat{\mu}_1||30) = (3-1||\hat{\mu}_{-1}||30) = -(30||\hat{\mu}_1||3-1) , \\ (3-1||\hat{\mu}_1||3-2) &= -(3-2||\hat{\mu}_{-1}||3-1) = (32||\hat{\mu}_1||31) = -(31||\hat{\mu}_{-1}||32) , \end{aligned}$$

and

$$(3-2||\hat{\mu}_1||3-3) = -(3-3||\hat{\mu}_{-1}||3-2) = (33||\hat{\mu}_1||32) = -(32||\hat{\mu}_{-1}||33) . \quad (23)$$

Due to the latter relations, the independent contributions to $(33||\hat{\mu}_1||33)_o$ reduce to six in total (cf. fig. 7). Differently from the 2_1^+ multiplet in fig. 5, the behaviour of these reduced brackets as a function of the lattice spacing is more multifaceted. In particular, the diagonal matrix element with maximum angular momentum projection (cf. the curve with diagonal crosses in fig. 7) follows a path that almost overlaps the one of the element $(30||\hat{\mu}_{-1}||31)$ (pentagons) throughout the considered interval of lattice spacing, displaying a local minimum at $a \approx 2.33$ fm, followed by a local maximum at $a \approx 2.67$ fm and a plateau in the large lattice-spacing region.

In the opposite direction, the two matrix elements undergo a steep increase with an inflection point at $a \approx 1.90$ fm, that eventually results in a plateau in the continuum limit. Both $(30||\hat{\mu}_{-1}||31)$ and $(33||\hat{\mu}_0||33)$ are most affected by discretization errors in the region $1.90 \lesssim a \lesssim 2.75$ fm.

Conversely, the diagonal matrix element with projection 2 (open circles) shows the smallest deviation from the exact matrix element, $\langle 3||\hat{\mu}||3 \rangle$ (dotted line), in the whole domain, except for a region $3.20 \lesssim a \lesssim 3.27$ fm. Regarding the 2_1^+ state, this fact remains true only in the interval $2.48 \lesssim a \lesssim 2.75$ fm (cf. open circles in fig. 5). However, in the two cases, the diagonal matrix elements with projection 2 drop to $\approx 0.10\mu_N$ at $a \approx 3.5$ fm.

A behaviour intermediate between the one of the $(33||\hat{\mu}_0||33)$ and $(32||\hat{\mu}_0||32)$ curves is found in the off-diagonal matrix elements $(33||\hat{\mu}_1||32)$ (open squares) and $(32||\hat{\mu}_1||31)$ (open triangles),

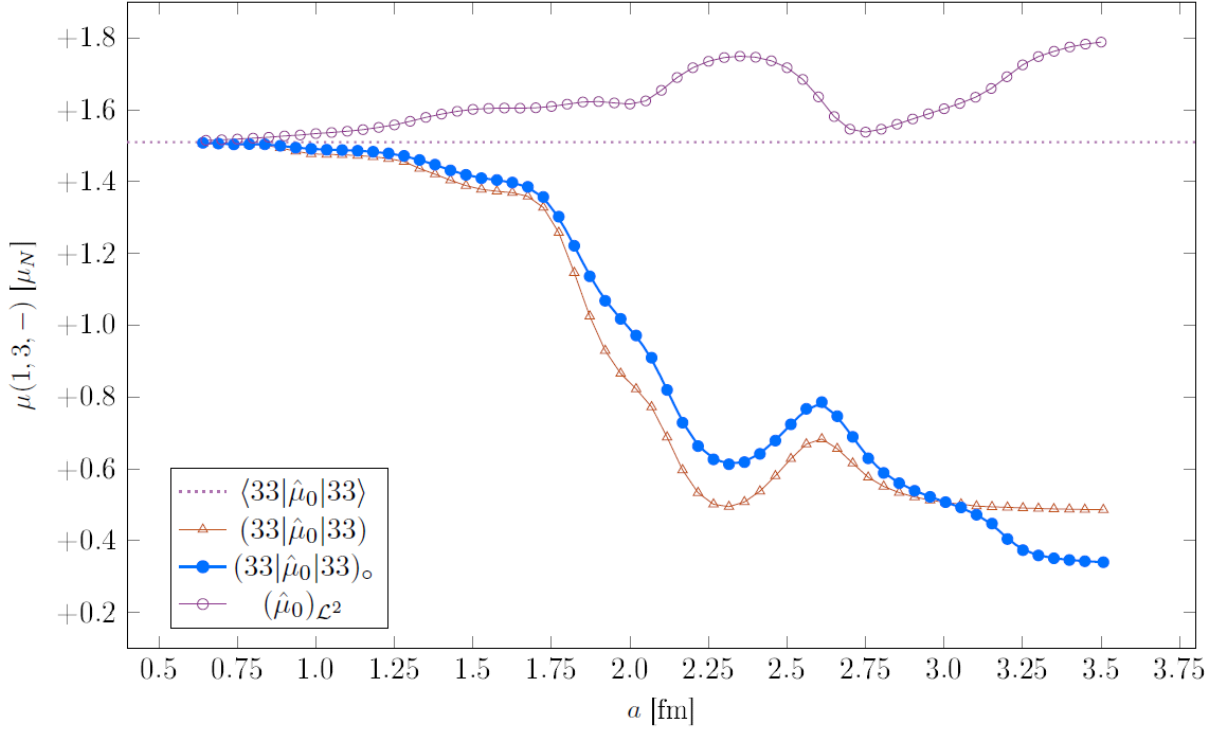


Figure 6: Average value of the magnetic dipole moment for the 3_1^- energy level of ^{12}C as a function of the lattice spacing. The broken line with circles denotes the estimated magnetic dipole moments obtained from the multiplet-averaged values of the squared total angular momentum operator, \mathcal{L}^2 [46, 140], over the five wavefunctions composing the 3_1^- level, degenerate in the continuum and infinite volume limit. The broken line with triangles denotes the matrix elements of the magnetic dipole moment operator over the lattice states with maximum projection along the z axis. The isotropically-averaged estimates of the same observable, extracted from the matrix element of $\hat{\mu}$ with lattice wavefunctions with different third component of the total angular momentum operator, are displayed by the broken lines with squares. The theoretical value at $1.5102 \mu_M$ is marked with a dotted line and reproduced with 10^{-3} precision by the values of $\langle 33|\hat{\mu}_0|33\rangle$ and $(33|\hat{\mu}_0|33)_o$ at $a \approx 0.64$ fm, equal to ≈ 1.5057 and $1.5081 \mu_N$ respectively. Finite-volume effects are suppressed by the constraint $Na \geq 19.5$ fm.

which indeed lie closest to the isotropic average (solid curve with full circles), except for intersection regions at 1.85 and 3.18 fm and in the stretch between the two local extrema. An inflection point is also detected around $a \approx 3.20$ fm, as for the $(32||\hat{\mu}_0||32)$ curve (cf. fig. 7).

Concerning the diagonal matrix element with projection 1 (vertical crosses), its curve displays a second local maximum at $a \approx 1.97$ fm, followed by another minimum at $a \approx 1.88$ fm, in contrast with all other reduced matrix elements. Additionally, its convergence to the continuum and infinite-volume value of $(31||\hat{\mu}_0||31)$ is the slowest among the brackets of the magnetic dipole moment operator, since 1% precision is reached only at $a \approx 0.85$ fm.

However, the two minima of the curve of the $(31||\hat{\mu}_0||31)$ bracket admit an interpretation on the basis of the range parameters η_1^{-1} and η_0^{-1} of the Ali-Bodmer potential [43], equal to 1.89 and 2.29 fm respectively. The probability density function associated with the lattice state $|31\rangle$, in fact, possesses local maxima that can be included in the lattice points when $a \approx \eta_1^{-1}$ (cf. sec. 2 of ref. [46]).

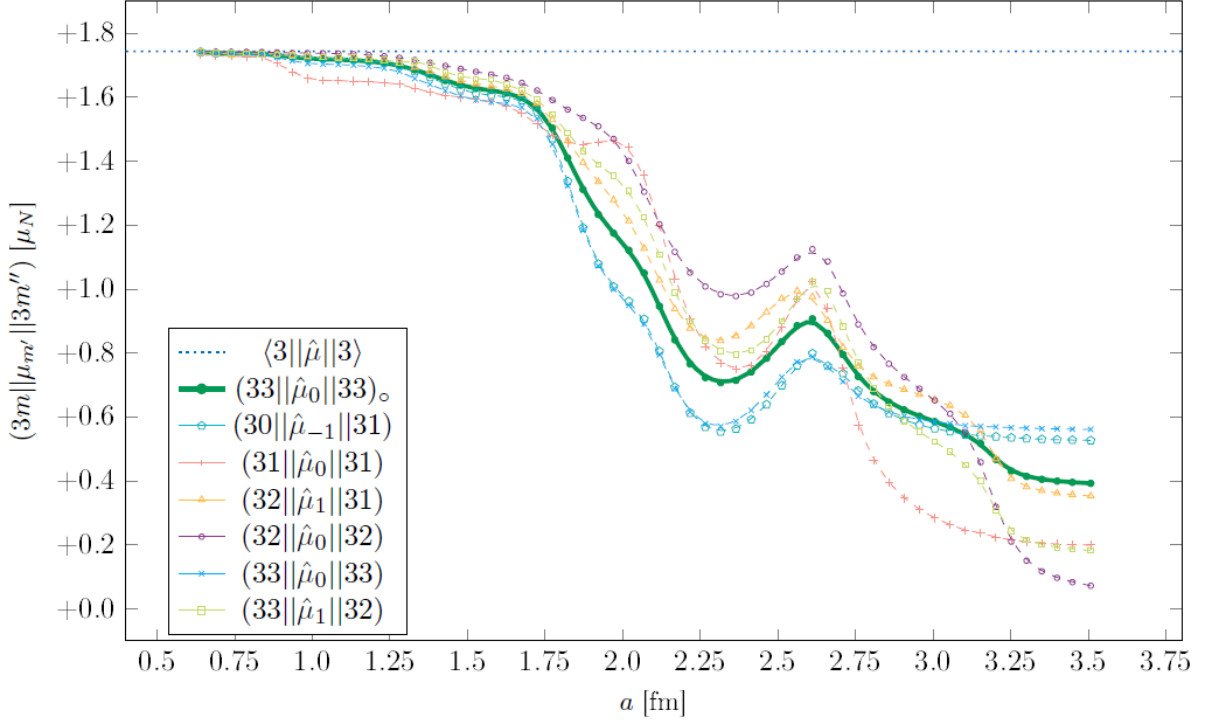


Figure 7: Behaviour of the reduced matrix elements between the spherical components of the magnetic dipole moment operator and lattice eigenstates with different angular momentum projection, m and m'' , along the z -axis as a function of the lattice spacing a for the 3_1^- state of ^{12}C . The listed matrix elements represent the nonvanishing independent contributions to the isotropically-averaged estimate of the magnetic dipole moment in eq. (18), divided by the Clebsch-Gordan coefficient $(313|mm'm'')$. The asymptotic value of the reduced matrix elements in the continuum and infinite volume limit is represented by a dotted line and is independent on the third component of the angular momentum. In particular, the dashed (solid and thick) curve with open (filled) circles represents the reduced (isotropically-averaged) magnetic dipole moment. The diagonal matrix elements $(32||\hat{\mu}_0||32)$ and $(31||\hat{\mu}_0||31)$ with intermediate projection are denoted by a dashed curve with vertical and diagonal crosses, lying above all other curves in the large lattice spacing region. Finally, the behaviour of the off-diagonal matrix elements $(30||\hat{\mu}_{-1}||31)$, $(32||\hat{\mu}_1||31)$ and $(33||\hat{\mu}_1||32)$ is described by lines with open pentagons, triangles and squares, respectively.

4. Conclusion

With the present work, we have complemented the vast literature on magnetic dipole moments [50, 71, 109], by paralleling the average values of this observable for even-even self-conjugate nuclei from ^{12}C to ^{44}Ti with the partitioning of nuclear matter into α -clusters. The measured gyromagnetic factors of excited states of these nuclei turn out to assume, within their errors, the same value of $g \approx +0.50$. It is shown that this specific feature can be explained on the basis of collective excitations of ^4He nuclei, neglecting the degrees of freedom of the single nucleons. Such macroscopic approaches are best suited to low-lying excited states located at the vicinity of α -decay thresholds.

The stability of the α -clusters has been further investigated for isotopes of the above chain of nuclei by appending one or two neutrons. Relying on Schmidt estimates [39], we confirmed that, in proximity of the shell closures $Z, N = 8$ and 20 the extra one or two neutrons determine the experimental g -factor values. The original positive values of the corresponding self-conjugate

nuclei undergo a significant reduction generated by the contribution of the negative g-factor of the additional neutrons. For the considered energy levels of the $N = Z + 1$ and 2 semi-magic nuclei in our chains, α -clustering is mitigated by the added neutrons. Outside the shell closures, for $N = Z + 2$ nuclei the added neutrons lose almost all their influence, and the predictions of eq. (4) are aligned with the experimental g-factors.

Spurred by the recent literature on the subject [44, 45, 46, 25], we have calculated the magnetic dipole moment of the 2_1^+ state at 4.44 MeV and the 3_1^- state at 9.64 MeV of ^{12}C in the framework of a macroscopic α -cluster model on the lattice in ref. [44]. Suppressing the finite-volume effects, we have analyzed the discretization artifacts through the behaviour of this observable as a function of the lattice spacing, ranging from $a \approx 0.65$ to 3.50 fm.

Unlike the energy (cf. fig. 32 in ref. [46]) or the squared angular momentum (cf. fig. 39 in ref. [46] and the curve with open circles in fig. 4), the magnetic dipole moment appears rather insensitive to discretization effects for $a \lesssim 2.0$ fm, where the artifacts amount to, at most, the 15% of the continuum and infinite-volume value, governed by eq. (3).

In particular, for the 2_1^+ state, the isotropic average, introduced in ref. [45], turns out not to improve significantly the estimate of the magnetic dipole moment provided by matrix element with maximum angular momentum projection along the lattice z -axis alone (cf. the curve with solid circles in fig. 4). The latter conclusion does not hold in the 3_1^- case, where the isotropic average turns out to improve sizably the estimate of this observable in the region with $a \lesssim 3.05$ fm (cf. fig. 6).

If its weak coupling to angular momentum symmetry breaking is confirmed in further nuclear systems on the lattice, the magnetic dipole moment evaluated at finite and sizable values of the lattice spacing (*e.g.* $a \sim 2.0$ fm) can corroborate the classification of lattice eigenstates in terms of $\text{SO}(3)$ quantum numbers, which is exact only in the continuum and infinite-volume limit.

Acknowledgements

We thank T. Otsuka for the shell-model calculation of the g-factors of the 2_1^+ states of ^{10}Be and ^{10}C . We gratefully acknowledge funding from the Deutsche Forschungsgemeinschaft (DFG, German Research Foundation) and the NSFC through the funds provided to the Sino-German Collaborative Research Center TRR110 ‘‘Symmetries and the Emergence of Structure in QCD’’ (DFG Project ID 196253076 - TRR 110, NSFC Grant No. 12070131001), the Chinese Academy of Sciences (CAS) President’s International Fellowship Initiative (PIFI) (Grant No. 2018DM0034), Volkswagen Stiftung (grant No. 93562), the European Research Council (ERC) under the European Union’s Horizon 2020 research and innovation programme (grant agreement No. 101018170) and the Espace de Structure Nucléaire Théorique (ESNT) of the CEA/DSM-DAM. The computational resources of the ‘‘CLAIX’’ cluster of the RWTH in Aachen (‘jara0015’ project, No. 24986) as well as the ones of the ‘‘Jean Zay’’ cluster of the IDRIS institute (CNRS, GENCI) in Orsay (DARI ‘dqt’ project, No. 102105/A0110513012) have been exploited.

Appendix

We here recapitulate the basic properties of the cubic group and the transformation tables for basis states of irreducible representations (irreps) of $\text{SO}(3)$ with $\ell \leq 9$ into the ones of \mathcal{O} (cf. ref. [140]).

E	$6C_2''$	$3C_4^2(\pi)$	$8C_3'$	$6C_4(\frac{\pi}{2})$
(0, 0, 0)	$(0, \pi, \frac{\pi}{2})$	$(\pi, \pi, 0)$	$(\frac{\pi}{2}, \frac{\pi}{2}, \pi)$	$(\frac{\pi}{2}, \frac{\pi}{2}, \frac{3\pi}{2})$
	$(0, \pi, \frac{\pi}{2})$	$(0, \pi, 0)$	$(\pi, \frac{3\pi}{2}, \frac{3\pi}{2})$	$(\frac{3\pi}{2}, \frac{\pi}{2}, \frac{\pi}{2})$
	$(0, \pi, \frac{3\pi}{2})$	$(\pi, 0, 0)$	$(\pi, \frac{3\pi}{2}, \frac{\pi}{2})$	$(\pi, \frac{\pi}{2}, \pi)$
	$(\frac{3\pi}{2}, \frac{\pi}{2}, \frac{3\pi}{2})$		$(\frac{3\pi}{2}, \frac{\pi}{2}, \pi)$	$(\pi, \frac{3\pi}{2}, \pi)$
	$(0, \frac{\pi}{2}, \pi)$		$(\pi, \frac{\pi}{2}, \frac{3\pi}{2})$	$(\frac{\pi}{2}, 0, 0)$
	$(\pi, \frac{\pi}{2}, 0)$		$(\frac{\pi}{2}, \frac{3\pi}{2}, \pi)$	$(\frac{3\pi}{2}, 0, 0)$
			$(\pi, \frac{\pi}{2}, \frac{\pi}{2})$	
			$(\frac{3\pi}{2}, \frac{3\pi}{2}, \pi)$	

Table 4: Representation of the group. The elements of each conjugacy class are listed in terms of Euler angles. For completeness, the symmetry operation (α, β, γ) consists of a rotation of angle γ about the z -lattice axis, followed by one of angle β about the y axis and by another of angle α about the z axis.

This group consists of 24 rotations about the symmetry axes of the regular hexahedron and the octahedron, partitioned into five equivalence classes. Adopting the notation by Schönflies [142], E represents the identity, $3C_4^2(\pi)$ the rotations of 180° about the three fourfold axes orthogonal to the faces of the cube, $6C_4(\pi/2)$ the 90° and 270° rotations about the latter axes (6 elements), $6C_2''$ the 180° rotations about the six diagonal axes parallel to two faces of the cube and $8C_3'(2\pi/3)$ are rotations of 120° and 240° about the four diagonal axes that cross two opposite vertexes of the cube (8 elements).

Furthermore, the characters of the five irreducible representations of \mathcal{O} are presented in tab. 4, together with the characters of $2\ell + 1$ -dimensional irreps of $\text{SO}(3)$.

Applying the great orthogonality theorem, the decomposition of the $2\ell + 1$ -dimensional representations of the rotation group into the $\#\mathcal{C}l$ cubic group irreps, is obtained (cf. tab. 5 and tab. II of ref. [44]),

$$D^\ell = \sum_{\oplus} q_\nu D^\nu, \quad (24)$$

where the multiplicity of the latter into the original irrep D^ℓ is denoted by

$$q_\nu = \frac{1}{|\mathcal{O}|} \sum_{i=1}^{\#\mathcal{C}l} |\mathcal{C}l_i| [\chi_i^\nu]^* \chi_i^\ell \quad (25)$$

In the last equation, the order of \mathcal{O} of the finite group is at the denominator, whereas χ_i^ν and χ_i^ℓ represent respectively the characters of the irreps of the cubic and the rotation group in the conjugacy class $\mathcal{C}l_i$ with $|\mathcal{C}l_i|$ elements. Moreover, the map between the basis states of $\text{SO}(3, \mathbb{Z})$ and $\text{SO}(3)$ irreps is provided by the projectors in eq. (40) of ref. [46].

Γ	E	$6C_2''$	$3C_4^2(\pi)$	$8C_3'$	$6C_4(\frac{\pi}{2})$
A_1	1	1	1	1	1
A_2	1	-1	1	1	-1
E	2	0	2	-1	0
T_1	3	-1	-1	0	1
T_2	3	1	-1	0	-1
D^ℓ	$2\ell + 1$	$(-1)^\ell$	$(-1)^\ell$	$1 - \text{mod}(\ell, 3)$	$(-1)^{[\frac{\ell}{2}]}$

Table 5: Character table of the cubic group. With the exception of the $\ell = 0, 1$ cases, this representation D^ℓ is fully reducible with respect to the \mathcal{O} operations.

Let $T_q^{(k)}$ denote the q component of a spherical tensor of rank $2k + 1$, the general component of the irreducible cubic tensor obtained from it is

$$T_q^{(\Gamma, k)} = \sum_{q'=-k}^k \sum_{g \in \mathcal{O}} \chi_\Gamma(g) D_{qq'}^k(g) T_{q'}^{(k)} \quad (26)$$

where the label k in the spherical tensor on the l.h.s. denotes the original irrep of $\text{SO}(3)$ from which it has been obtained, whereas the index q ranges from $-k$ to k . In contrast, the transpose transformation rule holds for the basis states of the two groups,

$$|\ell, \Gamma, m\rangle = \sum_{m'=-\ell}^{\ell} \sum_{g \in \mathcal{O}} \chi_\Gamma(g) D_{m'm}^\ell(g) |\ell, m'\rangle. \quad (27)$$

As a consequence of this descent in symmetry, in the cubic lattice environment the maximum rank of any irreducible tensor operator runs from one to three. As shown in sec. 4 of ref. [46] for the energy eigenstates, the non-null components q of $T^{(\Gamma, k)}$ and $|\Gamma\ell\rangle$, admixture of the $q \bmod 4$ components of their $\text{SO}(3)$ counterparts, can be unambiguously denoted with the I_z label. The ensuing distribution of m components of a spin- ℓ irrep into the (ℓ, Γ) irreps of $\text{SO}(3, \mathbb{Z})$ is known as *subduction* [143].

Furthermore, when the multiplicity coefficient q_Γ of the irrep Γ of \mathcal{O} is larger than one, further linear transformations on the outgoing states (cf. eq. (26)) or cubic tensor components (cf. eq. (27)) should be performed, in order to block-diagonalize the relevant projector and disentangle the repeated multiplets of states [140].

Eventually, for the construction of the tables (cf. tab. ??-17), the basis eigenfunctions for the '0' and '2' irreps of the cyclic group of order four, \mathcal{C}_4 , generated by an element of the conjugacy class $6C_4(\pi/2)$ of the cubic group (e.g. the counterclockwise rotation of $\pi/2$ about the z -axis of the cube) are assumed to be real, whereas the following phase convention

$$\begin{pmatrix} \Psi_{\Gamma, I_z=1} \\ \Psi_{\Gamma, I_z=3} \end{pmatrix} = -\frac{1}{\sqrt{2}} \begin{pmatrix} \Psi_\Gamma^{(p)} + i\Psi_\Gamma^{(q)} \\ -\Psi_\Gamma^{(p)} + i\Psi_\Gamma^{(q)} \end{pmatrix}. \quad (28)$$

for the basis state $\Psi_{\Gamma, I_z=1}$ ($\Psi_{\Gamma, I_z=3}$) belonging to the '1' ('3') irrep of \mathcal{C}_4 is understood.

Γ	ℓ	m	0
A_1	0	1	1

Γ	ℓ	m	1	0	1
T_1	0	1	1		
	1	1			1
	3	1			

Γ	ℓ	m	2	-2	-1	0	1	2
E	0	1						
	2	1	$\sqrt{1/2}$					$\sqrt{1/2}$
T_2	1	1					1	
	2	1	$i\sqrt{1/2}$					$-i\sqrt{1/2}$
	3	1						

Table 6: Decomposition tables for basis states of SO(3) with $\ell \leq 2$ into irreps of \mathcal{O} .

Γ	ℓ	m	-3	-2	-1	0	1	2	3
A_2	2	1	$i\sqrt{1/2}$					$-i\sqrt{1/2}$	
T_1	0	1				1			
	1	1	$\sqrt{5/8}$				$\sqrt{3/8}$		
	3	1			$\sqrt{3/8}$				$\sqrt{5/8}$
T_2	1	1	$\sqrt{3/8}$			$-\sqrt{5/8}$			
	2	1		$\sqrt{1/2}$				$\sqrt{1/2}$	
	3	1			$-\sqrt{5/8}$				$\sqrt{3/8}$

Table 7: Decomposition table for basis states of SO(3) with $\ell = 3$ into irreps of \mathcal{O} .

Γ	ℓ	m	-4	-3	-2	-1	0	1	2	3	4
A_1	0	1	$\frac{1}{2}\sqrt{5/6}$				$\frac{1}{2}\sqrt{7/3}$				$\frac{1}{2}\sqrt{5/6}$
E	0	1	$\frac{1}{2}\sqrt{7/6}$				$-\frac{1}{2}\sqrt{5/3}$				$\frac{1}{2}\sqrt{7/6}$
	2	1			$\sqrt{1/2}$				$\sqrt{1/2}$		
T_1	0	1	$i\sqrt{1/2}$								$-i\sqrt{1/2}$
	1	1		$\frac{1}{2}\sqrt{1/2}$				$\frac{1}{2}\sqrt{7/2}$			
	3	1				$\frac{1}{2}\sqrt{7/2}$				$\frac{1}{2}\sqrt{1/2}$	
T_2	1	1		$\frac{1}{2}\sqrt{7/2}$			$-\frac{1}{2}\sqrt{1/2}$				
	2	1			$i\sqrt{1/2}$				$-i\sqrt{1/2}$		
	3	1				$-\frac{1}{2}\sqrt{1/2}$				$\frac{1}{2}\sqrt{7/2}$	

Table 8: Decomposition table for basis states of SO(3) with $\ell = 4$ into irreps of \mathcal{O} .

$\Gamma \begin{array}{c} \ell \\ I_z \end{array} \backslash m$		$\ell = 5$										
		-5	-4	-3	-2	-1	0	1	2	3	4	5
E	0		$i\sqrt{\frac{1}{2}}$								$-i\sqrt{\frac{1}{2}}$	
	2				$i\sqrt{\frac{1}{2}}$				$-i\sqrt{\frac{1}{2}}$			
T_1	0		$\frac{1}{2}\sqrt{\frac{7}{6}}$				$\frac{1}{2}\sqrt{\frac{5}{3}}$			$\frac{1}{2}\sqrt{\frac{7}{6}}$		
	1			$-\frac{1}{4}\sqrt{\frac{7}{6}}$				$\frac{3}{4}$				$\frac{1}{4}\sqrt{\frac{35}{6}}$
	3	$\frac{1}{4}\sqrt{\frac{35}{6}}$				$\frac{3}{4}$				$-\frac{1}{4}\sqrt{\frac{7}{6}}$		
	0		$\frac{1}{2}\sqrt{\frac{5}{6}}$				$-\frac{1}{2}\sqrt{\frac{7}{3}}$			$\frac{1}{2}\sqrt{\frac{5}{6}}$		
	1			$\sqrt{\frac{5}{6}}$								$\sqrt{\frac{1}{6}}$
	3	$\sqrt{\frac{1}{6}}$								$\sqrt{\frac{5}{6}}$		
T_2	1			$\frac{1}{4}\sqrt{\frac{3}{2}}$				$\frac{\sqrt{7}}{4}$				$-\frac{1}{4}\sqrt{\frac{15}{2}}$
	2				$\sqrt{\frac{1}{2}}$				$\sqrt{\frac{1}{2}}$			
	3	$-\frac{1}{4}\sqrt{\frac{15}{2}}$				$\frac{\sqrt{7}}{4}$				$\frac{1}{4}\sqrt{\frac{3}{2}}$		

Table 9: Decomposition table for basis states of SO(3) with $\ell = 5$ into irreps of \mathcal{O} .

$\Gamma \begin{array}{c} \ell \\ I_z \end{array} \backslash m$		$\ell = 6$						
		-6	-5	-4	-3	-2	-1	0
A_1	0			$\frac{\sqrt{7}}{4}$				$-\sqrt{\frac{1}{8}}$
A_2	2	$\frac{1}{4}\sqrt{\frac{5}{2}}$				$-\frac{1}{4}\sqrt{\frac{11}{2}}$		
E	0			$\frac{1}{4}$				$\frac{1}{2}\sqrt{\frac{7}{2}}$
	2	$\frac{1}{4}\sqrt{\frac{11}{2}}$				$\frac{1}{4}\sqrt{\frac{5}{2}}$		
T_1	0			$i\sqrt{\frac{1}{2}}$				
	1				$\frac{1}{4}\sqrt{\frac{15}{2}}$			
	3		$\frac{1}{4}\sqrt{\frac{11}{2}}$				$-\frac{\sqrt{3}}{4}$	
T_2	1				$-\frac{1}{4}\sqrt{\frac{55}{14}}$			
	2	$i\frac{1}{4\sqrt{7}}$				$i\frac{1}{4}\sqrt{\frac{55}{7}}$		
	3		$\frac{1}{4}\sqrt{\frac{21}{2}}$				$\frac{1}{4}\sqrt{\frac{11}{7}}$	
	1				$\sqrt{\frac{2}{7}}$			
	2	$i\frac{1}{4}\sqrt{\frac{55}{7}}$				$-i\frac{1}{4\sqrt{7}}$		
	3						$\sqrt{\frac{5}{7}}$	

Table 10: Decomposition table for basis states of SO(3) with $\ell = 6$ and $m \leq 0$ into irreps of \mathcal{O} .

Γ	I_z	$\ell \backslash m$	6					
			1	2	3	4	5	6
A_1	0					$\frac{\sqrt{7}}{4}$		
A_2	2			$-\frac{1}{4}\sqrt{\frac{11}{2}}$				$\frac{1}{4}\sqrt{\frac{5}{2}}$
E	0					$\frac{1}{4}$		
	2			$\frac{1}{4}\sqrt{\frac{5}{2}}$				$\frac{1}{4}\sqrt{\frac{11}{2}}$
T_1	0					$-\mathrm{i}\sqrt{\frac{1}{2}}$		
	1		$-\frac{\sqrt{3}}{4}$				$\frac{1}{4}\sqrt{\frac{11}{2}}$	
	3				$\frac{1}{4}\sqrt{\frac{15}{2}}$			
T_2	1		$\frac{1}{4}\sqrt{\frac{11}{7}}$				$\frac{1}{4}\sqrt{\frac{21}{2}}$	
	2			$-\mathrm{i}\frac{1}{4}\sqrt{\frac{55}{7}}$				$-\mathrm{i}\frac{1}{4\sqrt{7}}$
	3				$-\frac{1}{4}\sqrt{\frac{55}{14}}$			
	1		$\sqrt{\frac{5}{7}}$					
	2			$\mathrm{i}\frac{1}{4\sqrt{7}}$				$-\mathrm{i}\frac{1}{4}\sqrt{\frac{55}{7}}$
	3				$\sqrt{\frac{2}{7}}$			

Table 11: Decomposition table for basis states of SO(3) with $\ell = 6$ and $m > 0$ into irreps of \mathcal{O} .

Γ	I_z	$\ell \backslash m$	7							
			-7	-6	-5	-4	-3	-2	-1	0
A_2	2			$\mathrm{i}\frac{1}{4}\sqrt{\frac{11}{3}}$				$\mathrm{i}\frac{1}{4}\sqrt{\frac{13}{3}}$		
E	0					$\mathrm{i}\sqrt{\frac{1}{2}}$				
	2			$\mathrm{i}\frac{1}{4}\sqrt{\frac{13}{3}}$				$-\mathrm{i}\frac{1}{4}\sqrt{\frac{11}{3}}$		
T_1	0					$\frac{1}{4}\sqrt{\frac{7}{5}}$				$\frac{1}{2}\sqrt{\frac{33}{10}}$
	1		$\frac{1}{8}\sqrt{\frac{65}{2}}$				$\frac{1}{8}\sqrt{\frac{77}{10}}$			
	3			$\frac{1}{8}\sqrt{\frac{7}{10}}$					$\frac{1}{8}\sqrt{\frac{231}{10}}$	
	0				$\frac{1}{4}\sqrt{\frac{33}{5}}$					$-\frac{1}{2}\sqrt{\frac{7}{10}}$
	1					$\frac{1}{2}\sqrt{\frac{3}{10}}$				
	3			$\frac{1}{3}\sqrt{\frac{33}{10}}$					$-\frac{1}{\sqrt{10}}$	
T_2	1		$\frac{3}{8}\sqrt{\frac{7}{2}}$				$-\frac{1}{24}\sqrt{\frac{143}{2}}$			
	2			$\frac{\sqrt{2}}{24}$				$\frac{1}{24}\sqrt{\frac{143}{2}}$		
	3				$-\frac{1}{24}\sqrt{\frac{13}{2}}$				$-\frac{1}{8}\sqrt{\frac{143}{6}}$	
	1					$-\frac{7}{12}\sqrt{2}$				
	2			$\frac{1}{12}\sqrt{\frac{143}{2}}$				$-\frac{\sqrt{2}}{24}$		
	3				$\frac{1}{6}\sqrt{\frac{11}{2}}$					$\frac{1}{\sqrt{6}}$

Table 12: Decomposition table for basis states of SO(3) with $\ell = 7$ and $m \leq 0$ into irreps of \mathcal{O} .

Γ	I_z	$\ell \backslash m$	7						
			1	2	3	4	5	6	7
A_2	2			$-i\frac{1}{4}\sqrt{\frac{13}{3}}$				$-i\frac{1}{4}\sqrt{\frac{11}{3}}$	
E	0					$-i\sqrt{\frac{1}{2}}$			
	2			$i\frac{1}{4}\sqrt{\frac{11}{3}}$				$-i\frac{1}{4}\sqrt{\frac{13}{3}}$	
T_1	0					$\frac{1}{4}\sqrt{\frac{7}{5}}$			
	1		$\frac{1}{8}\sqrt{\frac{231}{10}}$				$\frac{1}{8}\sqrt{\frac{7}{10}}$		
	3				$\frac{1}{8}\sqrt{\frac{77}{10}}$				$\frac{1}{8}\sqrt{\frac{65}{2}}$
	0					$\frac{1}{4}\sqrt{\frac{33}{5}}$			
	1		$-\frac{1}{\sqrt{10}}$				$\frac{1}{2}\sqrt{\frac{33}{10}}$		
	3				$\frac{1}{2}\sqrt{\frac{3}{10}}$				
T_2	1		$-\frac{1}{8}\sqrt{\frac{143}{6}}$				$-\frac{1}{24}\sqrt{\frac{13}{2}}$		
	2			$\frac{1}{12}\sqrt{\frac{143}{2}}$				$\frac{\sqrt{2}}{24}$	
	3				$-\frac{1}{24}\sqrt{\frac{143}{2}}$				$\frac{3}{8}\sqrt{\frac{7}{2}}$
	1		$\frac{1}{\sqrt{6}}$				$\frac{1}{6}\sqrt{\frac{11}{2}}$		
	2			$-\frac{\sqrt{2}}{24}$				$\frac{1}{12}\sqrt{\frac{143}{2}}$	
	3				$-\frac{7}{12}\sqrt{2}$				

Table 13: Decomposition table for basis states of SO(3) with $\ell = 7$ and $m > 0$ into irreps of \mathcal{O} .

Γ	I_z	$\ell \backslash m$	8								
			-8	-7	-6	-5	-4	-3	-2	-1	0
A_1	0		$\frac{1}{8}\sqrt{\frac{65}{6}}$				$\frac{1}{4}\sqrt{\frac{7}{6}}$				$\frac{\sqrt{33}}{8}$
E	0		$\frac{1}{8}\sqrt{\frac{455}{246}}$				$-\frac{1}{4}\sqrt{\frac{41}{6}}$				$\frac{1}{8}\sqrt{\frac{231}{41}}$
	2				$\frac{1}{4}\sqrt{\frac{273}{41}}$				$-\frac{1}{4}\sqrt{\frac{55}{41}}$		
	0		$\frac{3}{2}\sqrt{\frac{11}{82}}$								$-\frac{1}{2}\sqrt{\frac{65}{41}}$
	2				$\frac{1}{4}\sqrt{\frac{55}{41}}$				$\frac{1}{4}\sqrt{\frac{273}{41}}$		
T_1	0		$i\frac{1}{4\sqrt{57}}$				$i\frac{1}{4}\sqrt{\frac{445}{57}}$				
	1			$\frac{1}{8}\sqrt{\frac{57}{2}}$				$-\frac{3}{8}\sqrt{\frac{91}{38}}$			
	3					$\frac{5}{8}\sqrt{\frac{35}{114}}$				$\frac{1}{8}\sqrt{\frac{715}{114}}$	
	0		$i\frac{1}{4}\sqrt{\frac{445}{57}}$				$-i\frac{1}{4\sqrt{57}}$				
	1							$\frac{3}{2}\sqrt{\frac{5}{38}}$			
	3					$\frac{1}{2}\sqrt{\frac{13}{114}}$				$\sqrt{\frac{77}{114}}$	
T_2	1			$\frac{1}{8}\sqrt{\frac{71}{2}}$				$\frac{3}{8}\sqrt{\frac{273}{142}}$			
	2				$i\frac{3}{4}\sqrt{\frac{15}{142}}$				$i\frac{1}{4}\sqrt{\frac{1001}{142}}$		
	3					$-\frac{5}{8}\sqrt{\frac{35}{142}}$				$-\frac{1}{8}\sqrt{\frac{715}{142}}$	
	1							$\frac{1}{2}\sqrt{\frac{55}{142}}$			
	2				$i\frac{1}{4}\sqrt{\frac{1001}{142}}$				$-i\frac{3}{4}\sqrt{\frac{15}{142}}$		
	3					$\frac{1}{2}\sqrt{\frac{429}{142}}$				$-\sqrt{\frac{21}{142}}$	

Table 14: Decomposition table for basis states of SO(3) with $\ell = 8$ and $m \leq 0$ into irreps of \mathcal{O} .

Γ I_z		ℓ m	8							
			1	2	3	4	5	6	7	8
A_1	0					$\frac{1}{4}\sqrt{\frac{7}{6}}$				$\frac{1}{8}\sqrt{\frac{65}{6}}$
E	0					$-\frac{1}{4}\sqrt{\frac{41}{6}}$				$\frac{1}{8}\sqrt{\frac{455}{246}}$
	2			$-\frac{1}{4}\sqrt{\frac{55}{41}}$				$\frac{1}{4}\sqrt{\frac{273}{41}}$		
	0									$\frac{3}{2}\sqrt{\frac{11}{82}}$
	2			$\frac{1}{4}\sqrt{\frac{273}{41}}$				$\frac{1}{4}\sqrt{\frac{55}{41}}$		
T_1	0					$-\frac{1}{4}\sqrt{\frac{445}{57}}$				$-\frac{1}{4}\sqrt{\frac{1}{57}}$
	1		$\frac{1}{8}\sqrt{\frac{715}{114}}$				$\frac{5}{8}\sqrt{\frac{35}{114}}$			
	3			$-\frac{3}{8}\sqrt{\frac{91}{38}}$					$\frac{1}{8}\sqrt{\frac{57}{2}}$	
	0					$\frac{1}{4}\sqrt{\frac{1}{57}}$				$-\frac{1}{4}\sqrt{\frac{455}{57}}$
	1		$\sqrt{\frac{77}{114}}$				$\frac{1}{2}\sqrt{\frac{13}{114}}$			
	3			$\frac{3}{2}\sqrt{\frac{5}{38}}$						
T_2	1		$-\frac{1}{8}\sqrt{\frac{715}{142}}$				$-\frac{5}{8}\sqrt{\frac{35}{142}}$			
	2			$-\frac{1}{4}\sqrt{\frac{1001}{142}}$				$-\frac{3}{4}\sqrt{\frac{15}{142}}$		
	3				$\frac{3}{8}\sqrt{\frac{273}{142}}$				$\frac{1}{8}\sqrt{\frac{71}{2}}$	
	1		$-\sqrt{\frac{21}{142}}$				$\frac{1}{2}\sqrt{\frac{429}{142}}$			
	2			$\frac{3}{4}\sqrt{\frac{15}{142}}$				$-\frac{1}{4}\sqrt{\frac{1001}{142}}$		
	3				$\frac{1}{2}\sqrt{\frac{55}{142}}$					

Table 15: Decomposition table for basis states of SO(3) with $\ell = 8$ and $m > 0$ into irreps of \mathcal{O} .

Γ I_z		ℓ m	9									
			-9	-8	-7	-6	-5	-4	-3	-2	-1	0
A_1	0			$\frac{1}{4}\sqrt{\frac{7}{3}}$				$-\frac{1}{4}\sqrt{\frac{17}{3}}$				
A_2	2					$\frac{1}{4}\sqrt{\frac{13}{2}}$				$-\frac{1}{4}\sqrt{\frac{3}{2}}$		
E	0		$\frac{1}{4}\sqrt{\frac{17}{3}}$				$\frac{1}{4}\sqrt{\frac{7}{3}}$					
	2					$\frac{1}{4}\sqrt{\frac{3}{2}}$				$\frac{1}{4}\sqrt{\frac{13}{2}}$		
T_1	0			$\frac{7}{8}\sqrt{\frac{17}{690}}$				$\frac{1}{4}\sqrt{\frac{161}{30}}$				$-\frac{1}{8}\sqrt{\frac{429}{23}}$
	1				$\frac{1}{16}\sqrt{\frac{345}{2}}$				$\frac{3}{8}\sqrt{\frac{91}{230}}$			
	3		$\frac{1}{16}\sqrt{\frac{51}{230}}$				$\frac{41}{8\sqrt{138}}$				$-\frac{7}{16}\sqrt{\frac{143}{345}}$	
	0			$\frac{29}{8}\sqrt{\frac{2}{53015}}$				$\frac{1}{2}\sqrt{\frac{2737}{4610}}$				$\frac{7}{4}\sqrt{\frac{2431}{10603}}$
	1								$\frac{7}{8}\sqrt{\frac{9282}{53015}}$			
	3		$\frac{1}{2}\sqrt{\frac{461}{230}}$				$\frac{19}{4}\sqrt{\frac{17}{21206}}$				$\frac{11}{4}\sqrt{\frac{2431}{53015}}$	
	0			$\frac{1}{8}\sqrt{\frac{85085}{2766}}$				$-\frac{1}{4}\sqrt{\frac{715}{2766}}$				$\frac{3}{8}\sqrt{\frac{21}{461}}$
	1								$-3\sqrt{\frac{55}{922}}$			
	3						$\sqrt{\frac{1001}{2766}}$				$2\sqrt{\frac{35}{1383}}$	
T_2	1				$-\frac{1}{16}\sqrt{\frac{3}{10}}$				$-\frac{1}{8}\sqrt{\frac{91}{10}}$			
	2					$\frac{1}{4\sqrt{5}}$				$\frac{1}{4}\sqrt{\frac{39}{5}}$		
	3		$\frac{1}{16}\sqrt{\frac{255}{2}}$				$-\frac{1}{8}\sqrt{\frac{3}{2}}$				$-\frac{1}{16}\sqrt{\frac{429}{5}}$	
	1				$\frac{1}{2}\sqrt{\frac{13}{10}}$				$-\frac{1}{4}\sqrt{\frac{21}{10}}$			
	2					$\frac{1}{4}\sqrt{\frac{39}{5}}$				$-\frac{1}{4\sqrt{5}}$		
	3						$-\frac{1}{4}\sqrt{\frac{13}{2}}$				$\frac{1}{4}\sqrt{\frac{11}{5}}$	

Table 16: Decomposition table for basis states of SO(3) with $\ell = 9$ and $m \leq 0$ into irreps of \mathcal{O} .

Γ	I_z	ℓ m	9								
			1	2	3	4	5	6	7	8	9
A_1	0					$i\frac{1}{4}\sqrt{\frac{17}{3}}$				$-i\frac{1}{4}\sqrt{\frac{7}{3}}$	
A_2	2				$i\frac{1}{4}\sqrt{\frac{3}{2}}$				$-i\frac{1}{4}\sqrt{\frac{13}{2}}$		
E	0					$-i\frac{1}{4}\sqrt{\frac{7}{3}}$				$-i\frac{1}{4}\sqrt{\frac{17}{3}}$	
	2			$-i\frac{1}{4}\sqrt{\frac{13}{2}}$				$-i\frac{1}{4}\sqrt{\frac{3}{2}}$			
T_1	0					$\frac{1}{4}\sqrt{\frac{161}{30}}$				$\frac{7}{8}\sqrt{\frac{17}{690}}$	
	1		$-\frac{7}{16}\sqrt{\frac{143}{345}}$				$\frac{41}{8\sqrt{138}}$				$\frac{1}{16}\sqrt{\frac{51}{230}}$
	3			$\frac{3}{8}\sqrt{\frac{91}{230}}$					$\frac{1}{16}\sqrt{\frac{345}{2}}$		
	0					$\frac{1}{2}\sqrt{\frac{2737}{4610}}$				$\frac{29}{8}\sqrt{\frac{2}{53015}}$	
	1		$\frac{11}{4}\sqrt{\frac{2431}{53015}}$				$\frac{19}{4}\sqrt{\frac{17}{21206}}$				$\frac{1}{2}\sqrt{\frac{461}{230}}$
	3			$\frac{7}{8}\sqrt{\frac{9282}{53015}}$							
	0					$-\frac{1}{4}\sqrt{\frac{715}{2766}}$				$\frac{1}{8}\sqrt{\frac{85085}{2766}}$	
	1		$2\sqrt{\frac{35}{1383}}$				$\sqrt{\frac{1001}{2766}}$				
	3				$-3\sqrt{\frac{55}{922}}$						
T_2	1		$-\frac{1}{16}\sqrt{\frac{429}{5}}$				$-\frac{1}{8}\sqrt{\frac{3}{2}}$				$\frac{1}{16}\sqrt{\frac{255}{2}}$
	2			$\frac{1}{4}\sqrt{\frac{39}{5}}$				$\frac{1}{4\sqrt{5}}$			
	3				$-\frac{1}{8}\sqrt{\frac{91}{10}}$				$-\frac{1}{16}\sqrt{\frac{3}{10}}$		
	1		$\frac{1}{4}\sqrt{\frac{11}{5}}$				$-\frac{1}{4}\sqrt{\frac{13}{2}}$				
	2			$-\frac{1}{4\sqrt{5}}$				$\frac{1}{4}\sqrt{\frac{39}{5}}$			
	3				$-\frac{1}{4}\sqrt{\frac{21}{10}}$				$\frac{1}{2}\sqrt{\frac{13}{10}}$		

Table 17: Decomposition table for basis states of SO(3) with $\ell = 9$ and $m > 0$ into irreps of \mathcal{O} .

References

- [1] J.A. Wheeler, *Phys. Rev.* **52**, 1083-1106 (1937).
- [2] M. Freer, H. Horiuchi, Y. Kanada-En'yo, D. Lee and U.-G. Meißner, *Rev. Mod. Phys.* **90**, 3, 035004 (2018).
- [3] Y. Kanada-En'yo, *Clustering in light nuclei* in F. Gramegna, P. van Duppen, A. Vitturi and S. Pirrone, *Proceedings of the International Schhol of Physics "Enrico Fermi" Varenna* **201** / CCI, pag. 61-93, SIF Bologna (2019).
- [4] V. Somà, T. Duguet and C. Barbieri, *Phys. Rev. C* **84**, 064317 (2011).
- [5] V. Somà, L. Barbieri and T. Duguet, *Phys. Rev. C* **87**, 011303 (2013).
- [6] L.N. Cooper, *Phys. Rev.* **104**, 1189-1190 (1956).
- [7] V.G. Soloviev, *Nucl. Phys.* **9**, 655-664 (1958).
- [8] S. Typel, *Phys. Rev. C* **89**, 064321 (2014).
- [9] L. R. Hafstad and E. Teller, *Phys. Rev.* **54**, 681-692 (1938).
- [10] D.M. Brink and E. Boeker, *Nucl. Phys. A* **91**, pag. 1-26, 1 (1967).
- [11] P.H.C. Lau and N.S. Manton, *Phys. Rev. Lett.* **113**, 232503 (2014).
- [12] R. Bijker and F. Iachello, *Progr. in Part. and Nucl. Phys.* **110**, 103735 (2020).
- [13] C.J. Halcrow and J.I. Rawlinson, *Phys. Rev. C* **102**, 014314 (2020).
- [14] G. Stellin, L. Fortunato, A. Vitturi, *J. Phys. G* **8**, 085104 (2016).
- [15] L. Fortunato, G. Stellin, A. Vitturi, *Few-Body Systems* **58**, 19 (2017).

- [16] A. Vitturi, J. Casal, L. Fortunato and E.G. Lanza, *Phys. Rev. C* **101**, 014315 (2020).
- [17] R. Bijker and F. Iachello, *Ann. of Phys.* **298**, pag. 334-360, 2 (2002).
- [18] R. Bijker and F. Iachello, *Phys. Rev. Lett* **112**, 152501 (2014).
- [19] R. Bijker and f. Iachello, *Nucl. Phys. A* **957**, pag. 154-176, 1 (2017).
- [20] R. Bijker and F. Iachello, *Phys. Rev. C* **61**, 067305 (2000).
- [21] R. Bijker and F. Iachello, *Nucl. Phys. A* **1006**, 122077 (2021).
- [22] D. Jenkins, *J. Phys. G* **43**, 024003 (2016).
- [23] J. Casal, L. Fortunato, E.G. Lanza and A. Vitturi, *Eur. Phys. J. A* **57**, 33 (2021).
- [24] E. Epelbaum, H. Krebs, T.A. Lähde, D. Lee, and U.-G. Meißner, *Phys. Rev. Lett.* **109**, 252501 (2012).
- [25] S. Shen, T. A. Lähde, D. Lee and U.-G. Meißner, *Emergent geometry and duality in the carbon nucleus*, [ArXiv: 2202.13596](#) (2022).
- [26] H. Morinaga, *Phys. Rev.* **101**, 254 (1956).
- [27] K. Ikeda, N. Takigawa and H. Horiuchi, *Suppl. of Prog. in Theor. Phys. Extra Number*, 464-475 (1968).
- [28] K. Ikeda, H. Horiuchi and S. Saito, *Suppl. of Prog. in Theor. Phys.* **68**, 1-28 (1980).
- [29] G. J. Kumbartzki, K. Hagemeyer, W. Knauer, G. Krösing, R. Kuhnen, V. Mertens, K. -H. Speidel, J. Gerber and W. Nagel *Hyperfine Interactions* **7**, 253-264 (1979).
- [30] J. Asher, D.W. Bennett, H.A. Doubt, M.A. Grace, T.J. Moorhouse and B.J. Murphy, *J. Phys. G* **10**, 1079 (1984).
- [31] J. Leske, K.-H. Speidel, O. Kenn, S. Schielke and G. Müller, *Phys. Lett. B* **551**, 249-254 (2003).
- [32] A Kusoglu, A E Stuchbery, G Georgiev, A Goasduff, L Atanasova, D L Balabanski, M Bostan, M Danchev, P Detistov and K Gladnishki, *J. of Phys.: Conf. Ser.* **590**, 012041 (2015).
- [33] K.-H.Speidel, M.B.Goldberg, K.Hagemeyer, G.J.Kumbartzki, G.Goldring, Z.Shkedi, M.Schramm, G.Kraft and H.A.Doubt, *Phys. Lett. B* **57**, 2, 143-146 (1975).
- [34] K.-H. Speidel, S. Schielke, J. Leske, N. Pietralla, T. Ahn, A. Costin, M.v. Schmid, O. Zell, J. Gerber, P. Maier-Komor, S.J.Q. Robinson, A. Escuderos, Y.Y. Sharon and L. Zamick, *Phys. Lett. B* **659**, 101-106 (2008).
- [35] Y. Niv, M. Hass, A. Zemel and G. Goldring, *Phys. Rev. Lett.* **43**, 5, 326-330 (1979).
- [36] M. Mayr, K.-H. Speidel, M. Knopp, W. Karle, T. Faestermann, F. Hagelberg, H.-J. Simonis, P.N. Tandon and J. Gerber, *Zeitschr. für Physik A* **327**, 157-161 (1987).
- [37] S. Schielke, K.-H. Speidel, O. Kenn, J. Leske, N. Gemein, M. Offer, Y.Y. Sharon, L. Zamick, J. Gerber and P. Maier-Komor, *Phys. Lett. B* **567**, 153-158 (2003).
- [38] B.A. Brown, *Prog. in Part. and Nucl. Phys.* **47**, 517-599 (2001).
- [39] T. Schmidt, *Zeitschr. für Physik* **106**, 358 (1937).
- [40] M. Göppert Mayer and J.H.D. Jensen, *Elementary theory of nuclear shell structure*, J. Wiley & Sons, New York (1955).
- [41] R. Bijker and F. Iachello, *Phys. Rev. Lett.* **122**, 162501 (2019).
- [42] R. Bijker and F. Iachello, *Nucl. Phys. A* **1010**, 122193 (2021).
- [43] S.I. Fedotov, O. I. Kartavtsev, V. I. Kochkin and A. V. Malykh, *Phys. Rev. C* **70**, 014006 (2004).
- [44] B.N. Lu, T. A. Lähde, D. Lee and U.G. Meißner, *Phys. Rev. D* **90**, 034507 (2014).
- [45] B.N. Lu, T. Lähde, D. Lee and U.G. Meißner, *Phys. Rev. D* **92**, 014506 (2015).
- [46] G. Stellin, S. Elhatisari and U.-G. Meißner, *Eur. Phys. J. A* **54**, 228 (2018).
- [47] I. Talmi and A. De Shalit, *Nuclear Shell Theory*, Academic Press (1963).
- [48] E. Fiori, *Measurement of the magnetic moment of the 2+ state of ⁷²Zn via extension of the high-velocity transient-field method. Nuclear Theory, Doctoral Thesis*, Université Paris Sud - Paris XI (2010).
- [49] E. Tiesinga, P. Mohr, D. B. Newell and B. Taylor, *CODATA recommended values 2018*, *Rev. Mod. Phys.* **93**, 025010 (2020).
- [50] B. Castel and I.S. Towner, *Modern Theories on Nuclear Moments*, Oxford Studies in Nuclear Physics, Vol. 12, Oxford Science Publications (1990).

- [51] A. Poves, J. Sánchez-Solano, E. Caurier and F. Novacki, *Nucl. Phys. A* **694**, 157-198 (2001).
- [52] B.-A. Bian, Y.-M. Di, G.-L. Long, Y. Sun, J. Zhang and J. A. Sheikh, *Phys. Rev. C* **75**, 014312 (2007).
- [53] R.F. Garcia Ruiz, M. L. Bissell, K. Blaum et al. *Phys. Rev. C* **91**, 041304(R) (2015).
- [54] J. Carlson, S. Gandolfi, F. Pederiva, S.C. Pieper, R. Schiavilla, K.E. Schmidt and R.B. Wiringa, *Rev. Mod. Phys.* **87**, 1067-1118 (2015).
- [55] H. Krebs, *Eur. Phys. J. A* **56**, 9, 234 (2020).
- [56] B.A. Brown, *J. of Phys. G*, **8**, 679-685 (1982).
- [57] A. Saxena and P.C. Srivastava, *Phys. Rev. C* **96**, 024316 (2017).
- [58] K.-H. Speidel, *Hyperfine Interactions* **80**, 1205-1218 (1993).
- [59] K.-H. Speidel, O. Kenn and F. Nowacki, *Prog. in Part. and Nucl. Phys.* **49**, 1, 91-154 (2002).
- [60] A. Kusoglu, A.E. Stuchbery, G. Georgiev, B.A. Brown, A. Goasduff, L. Atanasova, D.L. Balabanski, M. Bostan, M. Danchev, P. Detistov, K.A. Gladnishki, J. Ljungvall, I. Matea, D. Radeck, C. Sotty, I. Stefan, D. Verney and D.T. Yordanov, *Phys. Rev. Lett.* **114**, 062501 (2015).
- [61] K.-H. Speidel, V. Mertens, W. Trölenberg, M. Knopp, H. Neuburger, J. Gerber and K. Bharuth-Ram, *Nucl. Phys. A* **403**, 2, 421-432 (1983).
- [62] K.-H. Speidel, V. Mertens, W. Trölenberg, M.Knopp, H. Neuburger, K. Bharuth-Ram and J. Gerber, *Zeitschr. für Phys. A* **315**, 319-323 (1984).
- [63] H. -J. Simonis, F. Hagelberg, K.-H. Speidel, M. Knopp, W. Karle, U. Kilgus and J. Gerber, *Zeitschr. für Phys. A* **330**, 361-364 (1988).
- [64] K.-H. Speidel, S. Schielke, J. Leske, J. Gerber, P. Maier-Komor, Y.Y. Sharon and L. Zamick, *Phys. Lett. B* **632**, 207-211 (2006).
- [65] B.A. Brown and W.A. Richter, *Phys. Rev. C* **74**, 034315 (2006).
- [66] W. Chung, *Empirical Renormalization of shell model Hamiltonians and magnetic dipole Moments of sd-shell Nuclei*, Ph.D. thesis, Michigan State University (1976).
- [67] B.H. Wildenthal, *Prog. in Part. and Nucl. Phys.* **11**, 5 (1984).
- [68] E.K. Warburton and B.A. Brown, *Phys. Rev. C* **46**, 923 (1992).
- [69] R. Hensler, J. W. Tape, J. Matthews, N. Benczer-Koller and J. R. MacDonald, *Phys. Rev. C* **10**, 919 (1974).
- [70] W.A. Richter, M.G. Van der Merwe, R.E. Julies and B.A. Brown, *Nucl. Phys. A* **523**, 325-353 (1991).
- [71] P.C. Zalm, J.F.A. van Hienen and P.W.M. Glaudemans, *Zeitschr. für Phys. A* **287**, 255-263 (1978).
- [72] D. Bazzacco, F. Brandolini, M. De Poli, P. Pavan, C. Rossi-Alvarez and R. Zannoni, *Phys. Rev. C* **29**, 1163 (1984).
- [73] W.L. Randolph, N. Ayres de Campos, J.R. Beene, J. Burde, M.A. Grace, D.F.H. Start and R.E. Warner, *Phys. Lett. B* **44**, 1, 36-38 (1973).
- [74] R.E. Horstman, J.L. Eberhardt, H.A. Doubt, C.M.E. Otten and G. van Middelkoop, *Nucl. Phys. A* **248**, 2, 291-316 (1975).
- [75] P. Goode, *Nuclear Physics A* **140** 481 -493 (1970).
- [76] B.H. Wildenthal and W. Chung in M. Rho and D. Wilkinson, *Mesons in Nuclei*, Vol. II, pag. 721, North Holland Elsevier, Amsterdam (1979).
- [77] W.E. Ormand and B.A. Brown, *Nucl. Phys. A* **491**, 1-23 (1989).
- [78] A. Arima, K. Shimizu, W. Bentz and H. Hyuga in J.W. Negele and E. Vogt, *Adv. Nucl. Phys.* **18**, 1 (1987).
- [79] S. Okabe, Y. Abe and H. Tanaka, *Prog. of Theor. Phys.* **57**, 3, 866-881 (1977).
- [80] V. Della Rocca and F. Iachello, *J. of Phys. G: Conf. Ser.* **966**, 012039 (2018).
- [81] M. Milin and W. von Oertzen, *Eur. Phys. J. A* **14**, 295-307 (2002).
- [82] Y. Sasamoto, T. Kawabata, T. Uesaka, K. Suda, Y. Maeda, S. Sakaguchi, K. Itoh, K. Hatanaka, M. Fujiwara, A. Tamii, Y. Shimizu, K. Nakanishi, K. Kawase, H. Hashimoto, Y. Tameshige, H. Matsubara, M. Itoh, H. P. Yoshida and M. Uchida *Mod. Phys. Lett. A* **21**, 31N33, 2393-2401 (2006).
- [83] S. Cohen and D. Kurath, *Nucl. Phys.* **73**, 1, 1-24 (1965).
- [84] M. Dufour and P. Descouvremont, *Nucl. Phys. A* **694**, 1-2, 221-232 (2001).

- [85] M. Dufour and P. Descouvemont, *Phys. Rev. C* **72**, 015801 (2005).
- [86] D.M. Brink, *The Alpha Particle Model of Light Nuclei* in C. Bloch, *Proceedings of the International Schhol of Physics "Enrico Fermi" Varenna* **36** / XXXVI, pag. 247-277, SIF Bologna, Academic Press, New York (1966).
- [87] H. Masui, K. Kato and K. Ikeda, *Phys. Rev. C* **73**, 034318 (2006).
- [88] T. Kawabata, Y. Sasamoto, M. Fujiwara, H. Hashimoto, K. Hatanaka, K. Itoh, M. Itoh, Y. Kanada-En'yo, K. Kawase, Y. Maeda, H. Matsubara, K. Nakanishi, S. Sakaguchi, Y. Shimizu, K. Suda, Y. Tameshige, A. Tamii, M. Uchida, T. Uesaka and H. P. Yoshida, *J. of Phys.: Conf. Ser.* **111**, 012013 (2008).
- [89] M. Milin, V.V. Ostashko, D. Miljanic, H.G. Bohlen, A. Di Pietro, O.Y. Goryunov, T. Kokalova, M. Lattuada, A. Musumarra, W. von Oertzen, M.G. Pellegriti, S. Romano, S. Thummerer, A. Tumino and M. Zadro, *Eur. Phys. J. A* **41**, 335-339 (2009).
- [90] S. Szpikowski and M. Trajdos, *Nucl. Phys. A* **272**, 1, 155-173 (1976).
- [91] A.G.M. van Hees, A.A. Wolters and P.W.M. Glaudemans, *Nucl. Phys. A* **476**, 1, 61-73 (1988).
- [92] W.M. Itano, *Phys. Rev. B* **27**, 1906 (1983).
- [93] V. Royden, *Phys. Rev.* **96**, 543 (1954).
- [94] J.R. Beene, J. Asher, N. Ayres De Campos, R.D. Gill, M.A. Grace and W.L. Randolph, *Nucl. Phys. A* **230**, 1, 141-152 (1974).
- [95] F. Adler and F.C. Yu, *Phys. Rev.* **81**, 1067 (1951).
- [96] F.A. Beck, T. Byrski, G.J. Costa and J.P. Vivien, *Phys. Rev. C* **16**, 2, 679-687 (1977).
- [97] P.M. Rowe, J. Asher, H.A. Doubt, M.A. Grace, P.D. Johnston and T.J. Moorhouse, *J. Phys. (Lond.) G* **4**, 431 (1978).
- [98] F. Adler and F.C. Yu, *Phys. Rev.* **82**, 105 (1951).
- [99] H. E. Weaver Jr., *Phys. Rev.* **89**, 923 (1953).
- [100] J.B. McGrory and B.H. Wildenthal, *Ann. Rev. Nucl. Part. Sci.* **30**, 383-436 (1980).
- [101] O. Lutz, A. Nolle and A. Schwenk, *Zeitschr. für Naturforsch. A* **28a**, 1370 (1973).
- [102] G. Wiechers and P.J. Brussaard, *Nucl. Phys.* **73**, 3, 604-612 (1965).
- [103] *Bulletin of the American Physical Society* **33**, 1564 (1988).
- [104] M. Micklinghoff, B. Castel and I.P. Johnstone, *Nucl. Phys. A* **251**, 1, 181-192 (1975).
- [105] W.L. Randolph Jr., R.R. Borchers, R. Michaelsen, D.W. Haag and W. Ribbe, *Phys. Rev. Lett.* **27**, 603 (1971).
- [106] E. Brun, J. Krausar, W.L. Pierce and W. J. Veigele, *Phys. Rev. Lett.* **9**, 166-167 (1962).
- [107] W. Kutschera, B.A. Brown and K. Ogawa, *Riv. Nuovo Cim.* **1**, 2, 1-116 (1978).
- [108] R. G. Cornwell and J. D. McCullen, *Phys. Rev.* **148**, 1157 (1966).
- [109] F. Brandolini, C. Rossi-Alvarez, C. Savelli, G. B. Vingiani and M. de Poli, *Lett. al Nuovo Cim.* **19**, 229-232 (1977).
- [110] P. Ring and P. Schuck, *The Nuclear Many-Body Problem*, pag. 60-65, 3rd Printing, Springer (2004).
- [111] K. Arai, Y. Ogawa, Y. Suzuki and K. Varga, *Phys. Rev. C* **54**, 132 (1996).
- [112] C. Yuan, T. Suzuki, T. Otsuka, F. Xu and N. Tsunoda, *Phys. Rev. C* **85**, 064324 (2012).
- [113] T. Suzuki, R. Fujimoto and T. Otsuka, *Phys. Rev. C* **67**, 044302 (2003).
- [114] M.R. Meder and J.E. Purcell, *Phys. Rev. C* **12**, 2056 (1975).
- [115] A. Poves and A. Zuker, *Phys. Rep.* **70**, 4 (1981).
- [116] S. Kahanna, H.C. Lee and C.K. Scott, *Phys. Rev.* **180**, 956 (1969).
- [117] R.D. Lawson, *Phys. Rev.* **124**, 1500 (1961).
- [118] N. Itagaki and S. Okabe, *Phys. Rev. C* **61**, 044306 (2000).
- [119] Y. Kanada-En'yo, H. Horiuchi and A. Doté, *Phys. Rev. C* **60**, 064304 (1999).
- [120] T. Suhara and Y. Kanada En'yo, *Phys. Rev. C* **82**, 044301 (2010).
- [121] N. Furutachi, M. Kimura, A. Doté, Y. Kanada-En'yo and S. Oryu, *Prog. of Theor. Phys.* **119**, 3, 403-420 (2008).
- [122] M. Dufour, P. Descouvemont, *Nucl. Phys. A* **726**, 1-2, 53-66 (2003).

- [123] I. Miyamoto and S. Ohkubo, *Zeitschr. für Phys. A* **349**, 297-299 (1994).
- [124] G. Lévai, *Phys. Rev. C* **88**, 014328 (2013).
- [125] Z. Fülöp, G. Lévai, E. Somorjai, Á.Z. Kiss, J. Cseh, P. Tikkanen and J. Keinonen, *Nucl. Phys. A* **604** (1996) 286-304.
- [126] T. Otsuka, private communication.
- [127] L. Liu and J. Li, *Sci. China Phys. Mech. and Astr.* **57**, 239-243 (2014).
- [128] T. K. Alexander, G. J. Costa, J. S. Forster, O. Häusser, A. B. McDonald, A. Olin and W. Witthuhn, *Phys. Rev. C* **9**, 1748 (1974).
- [129] K.-H. Speidel, G.J. Kumbartzki, W. Knauer, M. Knopp, V. Mertens, P.N. Tandon, J. Gerber and R.M. Freeman *Phys. Lett. B* **102**, 1, 6-8 (1981).
- [130] J.L. Eberhardt, R.E. Horstman, H.A. Doubt and G. van Middelkoop, *Nucl. Phys. A* **244**, 1, 1-14 (1975).
- [131] P.C. Zalm, A. Holthuizen, J.A.G. De Raedt and G. van Middelkoop, *Nucl. Phys. A* **315**, 1-2, 133-142 (1979).
- [132] S. Schielke, D. Hohn, K.-H. Speidel, O. Kenn, J. Leske, N. Gemein, M. Offer, J. Gerber, P. Maier-Komor, O. Zell, Y.Y. Sharon and L. Zamick, *Phys. Lett. B* **571**, 1-2, 29-35 (2003).
- [133] R. Ernst, K.-H. Speidel, O. Kenn, A. Gohla, U. Nachum, J. Gerber, P. Maier-Komor, N. Benczer-Koller, G. Kumbartzki, G. Jakob, L. Zamick and F. Nowacki, *Phys. Rev. C* **62**, 024305 (2000).
- [134] D. Suzuki, A. Shore, W. Mittig, J. J. Kolata, D. Bazin, M. Ford, T. Ahn, F.D. Becchetti, S. Beceiro Novo, D. Ben Ali, B. Bucher, J. Browne, X. Fang, M. Febbraro, A. Fritsch, E. Galyaev, A.M. Howard, N. Keeley, W. G. Lynch, M. Ojaruega, A. L. Roberts and X. D. Tang, *Phys. Rev. C* **87**, 054301 (2013).
- [135] H. Feldmeier, T. Neff, R. Roth and J. Schnack, *Nucl. Phys. A* **632**, 1, 61-95 (1998).
- [136] R. Roth, S. Reinhardt and H. Hergert, *Phys. Rev. C* **77**, 064003 (2008).
- [137] V. Gillet and N. Vinh Mau, *Nucl. Phys.* **54**, 321-351 (1964).
- [138] S. Ali and A.R. Bodmer, *Nuclear Physics* **80**, 99-112 (1966).
- [139] O. Portilho and S.A. Coon, *Zeitschr. für Physik A* **290**, 93 (1979).
- [140] G. Stellin, *Nuclear Physics in a finite volume: Investigation of two-particle and α -cluster systems* (doctoral thesis), Rheinische Friedrich-Wilhelms-Universität Bonn, Bonn (2020).
- [141] W. Greiner and J.A. Maruhn, *Nuclear Models*, Springer (1996).
- [142] L.R. Carter, *Molecular Symmetry and Group Theory*, John Wiley and Sons (1997).
- [143] J.J. Dudek, R.G. Edwards, M.J. Peardon, D.G. Richards and C.E. Thomas, *Phys. Rev. Lett.* **103**, 262001 (2009).